



Universiteit Utrecht

Bedform morphology under combined wave-current conditions in a nearshore environment

MSc thesis Earth, Surface, and Water,
Coastal dynamics and River systems
(37.5 ECTS)

Name: R.A. Schrijvershof, BSc. (3349446)
Date: 27 October 2014
1st supervisor: Prof. dr. B.G. Ruessink
2nd supervisor: Prof. dr. M.G. Kleinans
Version: 2

Abstract

The shape and geometry of bedforms in the nearshore zone strongly controls the turbulence and flow field above them, and as such, they determine the vertical sand concentration profile and with that the magnitude and direction of sediment transport. Understanding the relations between forcing and resultant bathymetry is therefore of crucial importance for coastal modelling purposes. The relationship between forcing and bedforms is, however, less understood for bedforms that are formed under the combined action of waves and currents (combined flows) than for pure waves or currents. To give insight in to the effect of a dynamic nearshore environment on combined flow bedform geometry, I studied the effect of changing hydrodynamics (within and between tidal cycles) on bedform morphology. Thereby, the accuracy of existing bedform geometry predictors is tested. A one-month measuring campaign was conducted at the beach of Egmond aan Zee to measure hydrodynamics together with small-scale sea-bed bathymetry, using a three-dimensional sonar ripple profiler (3DSRPLS). The sonar-acquired bathymetry images are processed in to Digital Elevation Models (DEMs) and classified in to four different bed states: small-scale 2D ripples, small-scale 3D ripples, large-scale bedforms, and super-positioned bedforms. Results show that a $\theta_c - \theta_w$ bed state stability diagram gives a good segregation of small-scale 2D ripples and large-scale bedforms, that small-scale 3D ripples are stable across a large range of the current strength, and that large-scale bedforms are formed under equal wave and current strengths. Tidal development of hydrodynamics and bedforms shows that bedform height shows a distinct post-high tide arrested development when large scale bedforms develop. This causes a decoupling of forcing and morphology, which is the reason that (a part of) the bedforms are not in equilibrium with the flow. I discuss that this out-of-equilibrium state is the main reason for the dis-ability of the equilibrium predictors to accurately predict bedform geometry. Therefore, future research on nearshore intertidal environments should specifically pay attention to hysteresis effects and its consequence for predicting geometry.

Table of Contents

Abstract.....	iii
1. Introduction.....	1
2. Theoretical background.....	3
2.1 Describing bedforms	3
2.2 Generic bedform classification	10
2.3 Bedform dynamics	17
2.3.1 Ripple ‘life cycles’	17
2.3.2 Response time and hysteresis.....	20
2.4 Modelling bedform geometry	22
2.4.1 Scaling relationships	22
2.4.2 Predicting combined flow bedform geometry.....	27
3 Methods.....	30
3.1 The study site	30
3.2 Instrumentation	32
3.3 Data processing.....	34
3.3.1 Hydrodynamics	34
3.3.2 Bed stress computations.....	35
3.3.3 Sonar image processing	36
3.1.1 Bed state classification.....	37
4 Results.....	40
4.1 Time series of hydrodynamics, bed stress, and morphology	40
4.2 The bedforms	41
4.2.1 Occurrence and characteristics.....	41
4.2.2 Generic classification.....	46
4.3 Bedform dynamics	49
4.3.1 Bedform response	49
4.3.2 Tidal relaxation	52
4.4 Equilibrium observations	54
4.5 Predicting bedform dimensions	55
5 Discussion.....	58
6 Conclusions.....	62
Acknowledgements.....	63
References.....	64

1. Introduction

The sea bed in the nearshore zone is often covered by bedforms. The morphology (i.e. shape and geometry) of these bedforms strongly controls the turbulence and flow field above them, and as such, determines to a large degree the structure of the bottom boundary layer (Grant and Madsen, 1986). Through the generation of near-bed turbulence, the bedforms determine the shape of the vertical sand concentration profile above them, and thereby the magnitude and direction of sediment transport (Masselink et al., 2007). The relevance of these bedforms with respect to flow dynamics and sediment transport rates have caused them to be of great interest to fluvial and coastal researchers. Consequently, a vast amount of literature is devoted to describing, quantifying and predicting the geometry, generation, development and destruction of bedforms under a range of hydrodynamic conditions. This has been done extensively for fluvial settings (unidirectional flow), marine and coastal settings (oscillatory flow), and, to a lesser extent, for environments where both types are present (combined flows). As a result, the effect of combined flows on bedform morphology is known to a lesser extent than under solely unidirectional or oscillatory flow. Nonetheless, the conditions in natural occurring environments are rarely pure wave- or current-dominated but rather affected by both.

The bedforms on the intertidal stretch of a sandy beach can be subjected to the combined action of waves and currents when a strong longshore current is provoked by oblique incident waves. The relation between wave-current bedform morphology and hydrodynamic forcing is, however, only studied in laboratory settings (Arnott and Southard, 1990; Khelifa and Ouellet, 2000; Dumas et al., 2005) and in field settings such as deep water continental shelf environments (Amos et al., 1988; Tanaka and Shuto, 1984; Li and Amos, 1996, Soulsby et al., 2012). The conditions on an intertidal beach, however, are not comparable to these environments because the strength of the currents and the waves can be larger and the conditions change fast due to rising and falling waters, which can cause lag effects (hysteresis) in bedform development. Of these previous studies, the laboratory experiments gave detailed measurements of combined flow bedform configuration. With that they developed boundaries for the geometry of combined flow bedforms, such as the minimum and maximum values of the ripple index (RI), symmetry index (SI), and the roundness index (RDI). The field and laboratory studies have, co-operatively, led to combined flow ripple classification schemes (Amos et al., 1988; Arnott and Southard, 1990; Van Rijn, 1993; Li and Amos, 1996) which relate stable bedform type to hydrodynamic forcing. A few researchers have also put effort in developing combined flow bedform geometry predictors (Li et al., 1996; Khelifa and Ouellet, 2000; Soulsby and Whitehouse, 2005). Although these predictors were shown to perform better in predicting combined flow bedform geometry than pure wave or current predictors, the field data for testing the predictors is very limited. Because no research is done on combined flow bedform morphology on a sandy intertidal beach, it is unknown how these predictors perform in such an environment.

The prediction of combined flow bedform geometry requires knowledge on the processes, initial, and boundary conditions that determine bedform type and characteristics, such as height, length, orientation, and three-dimensionality. To reveal the formative processes of combined-flow bedform geometry in the nearshore, the bedform types are placed in generic bedform stability diagrams. Furthermore, the development of the bedforms during a tidal cycle is examined and it is investigated whether the morphology of the bedforms shows lag effects with the hydrodynamic forcing. A final objective of the thesis is to explore how the existing bedform geometry predictors perform for the bedforms found during the field campaign.

Clearly, a gap exists in the knowledge on the behaviour of combined-flow bedforms in the nearshore. Therefore, the main objective of this thesis is to examine the characteristics and dynamics of combined flow bedforms on a sandy intertidal beach and test the available bedform geometry predictors. The main research question that follows is: what is the effect of a nearshore environment on the dynamics of combined flow bedform configuration? An answer is sought by investigating the following sub-research questions:

1. What are the main characteristics in configuration (type, height, and wavelength) of bedforms that are formed under the influence of the combined action of waves and currents in a nearshore environment?
 - a. What type of bedforms can be found in the setting of the present study?
 - b. What are the characteristic properties of these bedforms?
2. How does bedform geometry change when hydrodynamic conditions change during rising and falling water?
 - a. Which hydrodynamic parameters are the leading factors that determine bedform morphology?
 - b. How does the morphology of the bedforms change when these parameters change?
 - c. Is the morphology of the ripples subjected to hysteresis effects?
3. Do the existing equilibrium bedform geometry predictors perform well for the present environment?

This thesis is organized as follows: a review of the established knowledge on describing bedforms, bedforms classification schemes, scaling relationships and prediction of bedform geometry will be given in Chapter 2. Secondly, the field site and methods used to obtain, process and analyze the data are described in Chapter 3. The results are presented in Chapter 4 where after a comparison with the bedform literature and a discussion of the results is given in Chapter 5. The finalizing conclusions of the thesis are presented in Chapter 6.

2. Theoretical background

Ripples are considered to be small-scale bedforms with heights up to approximately 0.1 m and spacing up to approximately 1 m. They are the dominating type of bedforms in the nearshore zone, i.e., the shoaling-, surf-, and swashzone. These regions are affected by waves generated by the wind, and currents that arise from multiple mechanisms like cross-shore return flows, geostrophic flows, and the tide. Consequently, the ripples at the coast may be formed by waves and currents that act under varying strengths and varying angles. This causes the ripples in coastal regions to vary widely in time and space. An accurate description of the configuration (i.e., geometry, morphology, and three-dimensionality) of these ripples is essential for studying the profiles and the dynamics of ripple morphology in the nearshore. These topics will be evaluated below by analyzing the procedures and schemes that are developed for current bedforms, wave bedforms, and combined-flow bedforms.

2.1 Describing bedforms

Cross-sectional geometry

Describing the geometry of ripples is a first step in analyzing the characteristics of ripples. The geometry is most often described by the ripple trough-to-crest height (η) and ripple spacing, or wavelength (λ). The wavelength is usually used as an indicator between different types of bedforms. Besides the ripple height and wavelength, a number of ratios are used to further define ripple morphology (Dumas et al., 2005). These are: the ripple index (RI), that gives an indication of the steepness of the ripple

$$\left(RI = \frac{\eta}{\lambda} \right) \quad (1)$$

the symmetry index (SI), that quantifies the degree of asymmetry of the bedform

$$\left(SI = \frac{stoss}{lee} \right) \quad (2)$$

and the roundness index (RDI), which expresses the degree of convexity of the stoss side of the ripple

$$\left(RDI = \frac{a}{b} \right) \quad (3)$$

The parameters used to describe cross-sectional bedform geometry and to calculate equation 1,2 and 3 are visualized in Figure 1.

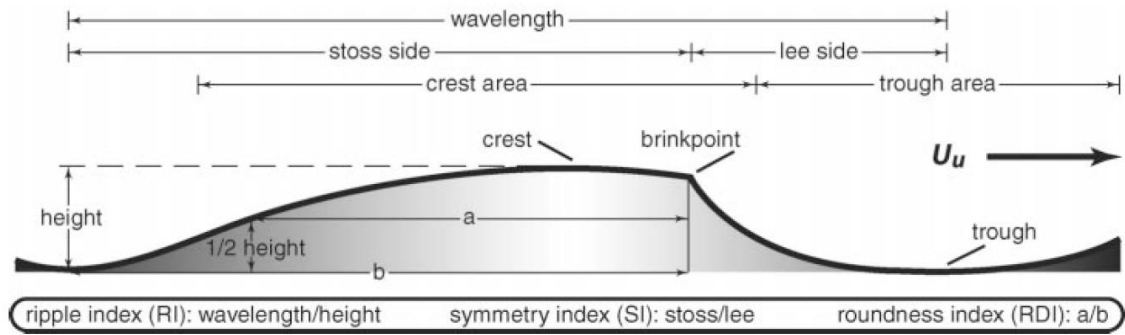


Figure 1: Parameters to describe cross-sectional ripple geometry (Dumas et al., 2005).

Experimental (laboratory) work on bedform geometry under combined flows has provided in equilibrium ranges for these ratios that specify particular ripples. Table 1 lists the ranges of these ratios for specific ripple types. The ranges do not always correspond with one another and consequently, do not provide robust threshold values to distinguish between ripple types. They do however, provide a first approximation for the determination of ripple type. It was found that:

- current ripples are well separated by the symmetry index, i.e., they are characterized by a strong asymmetry (Yokokawa, 1995).
- The ripple index is of limited use in differentiating between combined flow and oscillatory ripples (Dumas et al., 2005).
- Combined flow ripples are well distinguished by their rounded profile, i.e., high RDI values (Yokokawa, 1995).

It was suggested that a boundary between wave-dominated and current-dominated combined flow ripples may lie at $RDI = 0.54$. Wave ripples all had a RDI of less than 0.45. In a plot of the roundness index versus the ratio of the two velocity components it was found that the combined flow ripples become more rounded with decreasing strength of the oscillatory component (Yokokawa, 1995).

General features of the three kind of ripples are that current ripples have an asymmetric shape with sharp brinkpoints, wave ripples are predominantly symmetrical with sharp crests, and combined flow ripples are composed of superimposed wave and current ripples of roughly equal magnitudes (Li and Amos, 1996)

Besides these parameters that quantify the cross-sectional geometry of ripples, other descriptions are used to characterize the ripples. These are orientation, migration rate, and planform geometry (or morphology). Smyth and Li (2005) analyzed the orientation and migration rates of ripples. They concluded that bedforms were predominantly aligned with the waves, and migrated primarily in the direction of the waves, but occasionally changed direction under opposing currents. The morphology will be discussed next.

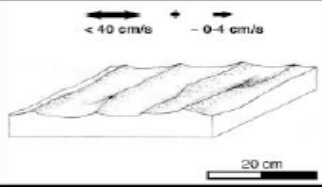
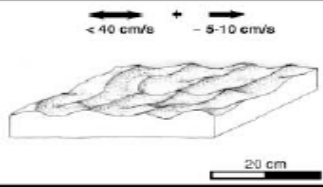
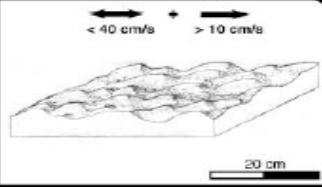
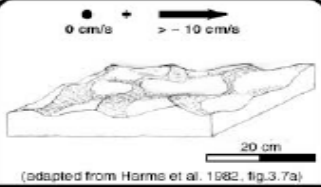
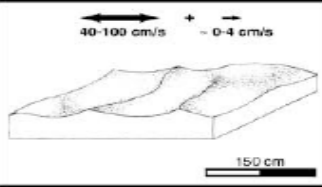
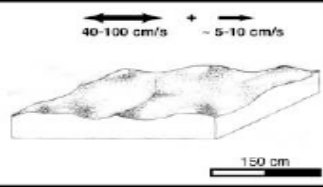
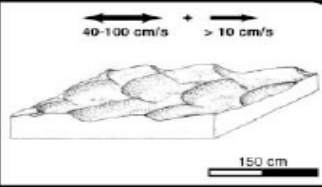
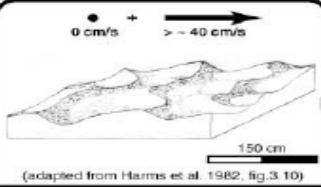
Morphology

Describing the morphology of bedforms in an objective and descriptive manner is often the most difficult quantity to specify because of the large variations in type, dimensions, and origin (Dumas et al., 2005). Consequently, there is at the moment no universal scheme for describing ripple morphology for current, wave and combined flow ripples. Figure 2 illustrates the terms that are used to describe the crest lines of ripples that are formed under unidirectional flow. They may be straight, sinuous, catenary, linguoid or lunate (Simons and Richardson, 1966). The sequence of bedform types found in coastal zones is shown in Figure 3. The sedimentary structures that are produced by waves in the nearshore are symmetric ripples. The bedforms develop in a consistent pattern, showing increasing asymmetry with decreasing cross-shore distance to the beach. The ripple types that are discriminated in the coastal zone are linear, irregular, cross-ripples, and mega-ripples (Clifton, 1976).

Moreover, the sequence of bedform types that are formed during a storm cycle was analyzed during a field study by Hay and Mudge (2005). In a nearshore sandy seabed, at ~3 m waterdepth and with a 150 μm median grain diameter, they identified irregular ripples, cross ripples, linear transition ripples, lunate megaripples, and flat bed. A clear repeated occurrence of the bed state cycle could be associated with each storm event. At the onset of each event, the bed state sequence progressed from irregular ripples, to cross ripples, to linear transition ripples, and subsequently evolved to flat-bed during intense wave energies. The occurrence of these bed states was found to be a strong function of incident wave energy, with each bed state occurring within a relatively narrow range of the sea- and swell energies. During storm wave decay this sequence of bed state reversed. They discuss that the reversal of this sequence during storm wave decay indicates a lack of significant dependence on prior bed state because the bed adjusts to changes in wave forcing.

Multiple schemes have been proposed for the classification of ripples formed under the combined action of waves and currents. The discrimination between types of ripples that are formed by combined flows is generally based on the degree of influence from waves or currents. Pioneer (field) work on combined flow bedform geometry was conducted by Amos et al. (1988). They visually identified six types of ripples at a continental shelf environment where waves and steady currents were generally orthogonal: wave ripples (W), transitional wave ripples (Wc), wave-current ripples (WC), transitional current ripples (Cw), straight-crested current ripples (Cs), and linguoid current ripples (Cl). Besides these ripple types, poorly developed ripples and flatbed were found. Another field study, also based on ripple data from a continental shelf environment, proved that the ratios of the skin-friction wave to current shear velocity (u_{*ws}/u_{*cs}) can be used to separate combined flow ripples (Li and Amos, 1996). During this fieldwork the peak tidal flows were generally to the northeast and southwest and waves approached generally from the south and southwest. The ripples were separated as:

Table 1: Classification of sand ripples by size, symmetry and flow conditions. Classification is based on: experimental data of Dumas et al. (2005), using grain sizes of 0.11 mm (very fine) and 0.17 mm (fine), wave periods of 9.4 and 7 s, and a super imposed oscillatory flow at 0° or 180° with respect to the current; flume data of Yokokawa (1995), where wave and currents also acted at 0° or 180°; and data from Harms (1969); Allen (1985a); and Bogge (2001). (figure from Dumas et al., 2005)

SMALL-SCALE BED FORMS: $\lambda < 20$ cm				
Bed form	Symmetric small ripples (SSR) regular, 2D, symmetrical, sharp crests, straight flanks, broad troughs	SSR + asymmetric small ripples (ASR) more irregular, 2-2.5D, still symmetrical, rounder crests, some straight and some biconvex flanks	ASR + asymmetric large ripples irregular, 3D, asymmetrical, larger λ and height, round biconvex profiles, pronounced scour on lower end of stoss	Current ripples very irregular, 3D, sharp crests, steep and straight lee, convex-up stoss
Symmetry index	-1.2	-1.5		5-10 (Yokokawa 1995)
Dip of lee side	11-18°		24-27° dip of lee side increases with increasing U_b	- angle of repose (30-35°)
Roundness index	0.44	-0.50	> 0.50	0.5-0.6 (Yokokawa 1995)
Ripple index	generally between 8-12 for all bed forms			
Orbital diameter/wavelength	8-15	- 8-15	8-15	N/A
LARGE SCALE BED FORMS: $\lambda > 100$ cm				
Bed form	Symmetric large ripples (SLR) SLR: 2.5D, symmetrical, sharp discontinuous crests = to brink, straight flanks	Hummocky (HM) + SLR + ALR HM: 3D, symmetrical, no brink point, broad round crests, domal, convex-up flanks	Asymmetric large ripples (ALR) ALR: 2D-3D, asymmetrical, brink not always = to crest, round stoss with break in slope, can have scour pits on lower end of stoss	Dunes regular (2D) to irregular (3D), sharp crests, steep and straight lee, straight to convex-up stoss
Symmetry index	-1.0 (≤ 1.5)	≤ 2	> 2	-
Dip of lee side	14-24° (SLR), 15-29° reverse large ripples (RLR)		23-31° dip of lee side increases with increasing U_b	- angle of repose (30-35°)
Roundness index	- 0.40-0.50 highest for HM bed forms	- 0.45-0.60	- 0.55-0.75 (up to 0.95)	-
Ripple index	generally between 8-12 for all bed forms			
Orbital diameter/wavelength	1-2	1-2	1-2	N/A

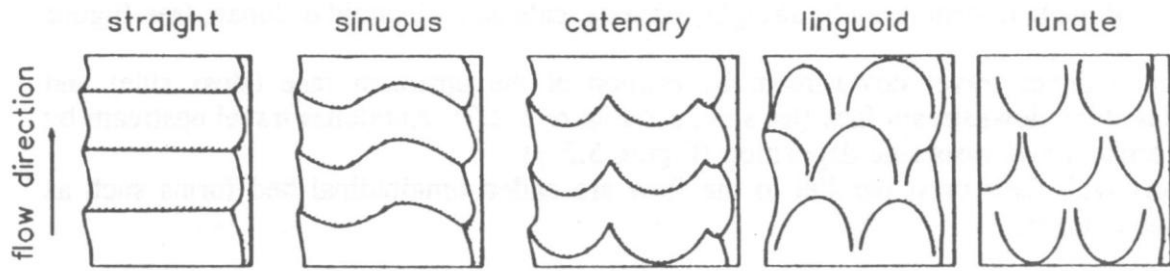


Figure 2: Ripple types under unidirectional flow (Simons and Richardson, 1966)

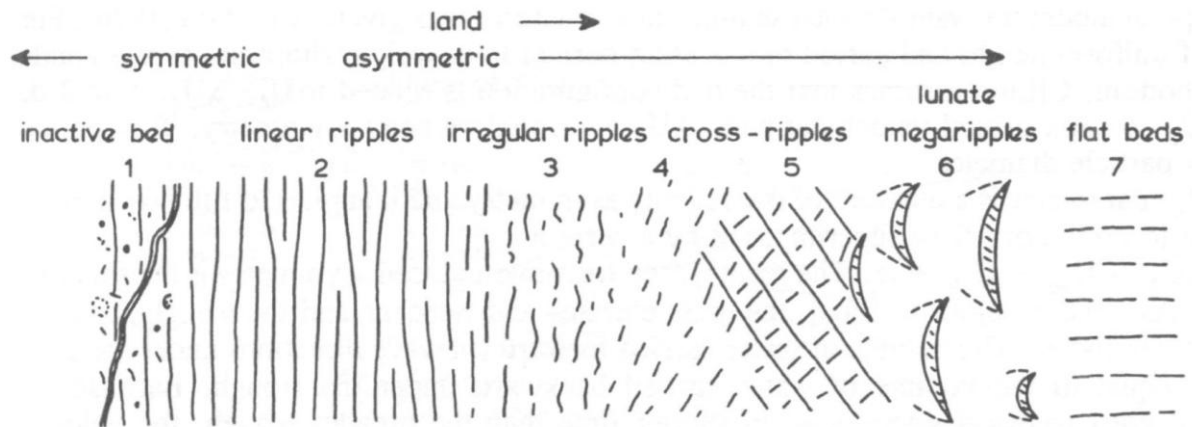


Figure 3: Bedform sequence in coastal zones (Clifton, 1976).

$$\left(\frac{u_{*WS}}{u_{*CS}}\right) > 1.25 \quad \text{Wave-dominant}$$

$$0.75 < \left(\frac{u_{*WS}}{u_{*CS}}\right) < 1.25 \quad \text{Wave-current}$$

$$\left(\frac{u_{*WS}}{u_{*CS}}\right) < 0.75 \quad \text{Current-dominant.}$$

Flume experiments on combined flow ripple geometry for waves and currents under an angle of 90° were performed by Andersen and Faraci (2002). They differentiated between regular, serpentine, segmented and irregular bedform shapes. A classification of these ripple types was given, based on the ratio of the unidirectional and oscillatory velocities:

$$\frac{u_c}{u_w} < 0.2 \quad \text{Wave dominated straight crested regular pattern, normally to the waves}$$

$$0.3 < \frac{u_c}{u_w} < 0.6 \quad \text{Serpentine morphology}$$

$$0.65 < \frac{u_c}{u_w} < 1.1 \quad \text{Segmented}$$

$$1.1 < \frac{u_c}{u_w} \quad \text{Irregular}$$

The morphologic classification of Andersen and Faraci (2002) is not equal to that of Li and Amos (1996), however, both classifications show the importance of the relative strength of the current. Apparently, the relative strength of the currents (or the waves) is an important factor for the resultant morphology. This may account for field conditions, where the angle varies as a function of time, as well as lab conditions where the angle is fixed during the experiment. Young and Sleath (1990) also performed laboratory experiments with waves perpendicular to a current. Their measurements of ripple geometry, using cohesion-less sand with median diameters of 0.203, 0.445, 0.700, and 1.065 mm, showed that an increasing superimposed steady current induces a waviness of the crest line of the ripples. A serpentine pattern will develop when the steady current exceeds a limit of $\frac{U_\infty}{U_{*c}} < 31$ if U_∞ is less than 0.38 m/s, where U_∞ is the amplitude of the velocity of the oscillating tray used in the experiment and U_{*c} is the shear velocity just upstream of the tray, which is an analogue for the strengths of the waves and the currents, respectively.

Dumas et al. (2005) proposed a division of combined flow ripples on wave length; short wave ripples (SWR, $\lambda < 20$ cm) versus long wave ripples (LWR, $\lambda > 100$ cm). It was found that the wavelength of combined flow ripples is bimodal, there are hardly any ripples with wavelengths between 20 and 100 cm. The ripples were further classified based on symmetry; symmetric versus asymmetric. In Table 1 this division is used. The ripples are classified to the degree of formation by waves, currents, or combined flows, the wavelength, and the symmetry. This diagram is at the moment the most all-embracing diagram to classify ripples that are formed under either wave, current, or combined flow action.

Three-dimensionality

Table 1 lists another property of ripples not discussed so far. The small-scale bedforms are assigned 2D for wave-dominant conditions, 2,5D-3D for combined flow conditions, and 3D for current-dominant conditions. This label refers to the number of dimensions that is needed to describe the full morphology of the ripple. In general wave ripples do not vary substantially in the direction perpendicular to the direction of wave propagation. Hence, a cross-sectional view (2D) would be sufficient to describe the bedforms (Figure 4A). A super imposed increasing unidirectional current increases the discontinuity of the crestlines of the ripples (figure 4B). A cross-sectional view will not suffice in describing the morphology of the ripples anymore, a three-dimensional description is required (Figure 4C). Dumas et al. (2005) found in their experiments, with following and opposing flow, that the combined flow ripples evolve to 3D when the steady current reaches a strength of 0.10 - 0.15 m/s. Additionally, they found that the runs with the finer sediments showed better developed oscillatory and combined flow 3D ripples, in contrast to the development of 2D ripples. This was already found for oscillatory ripples by Southard et al. (1990).

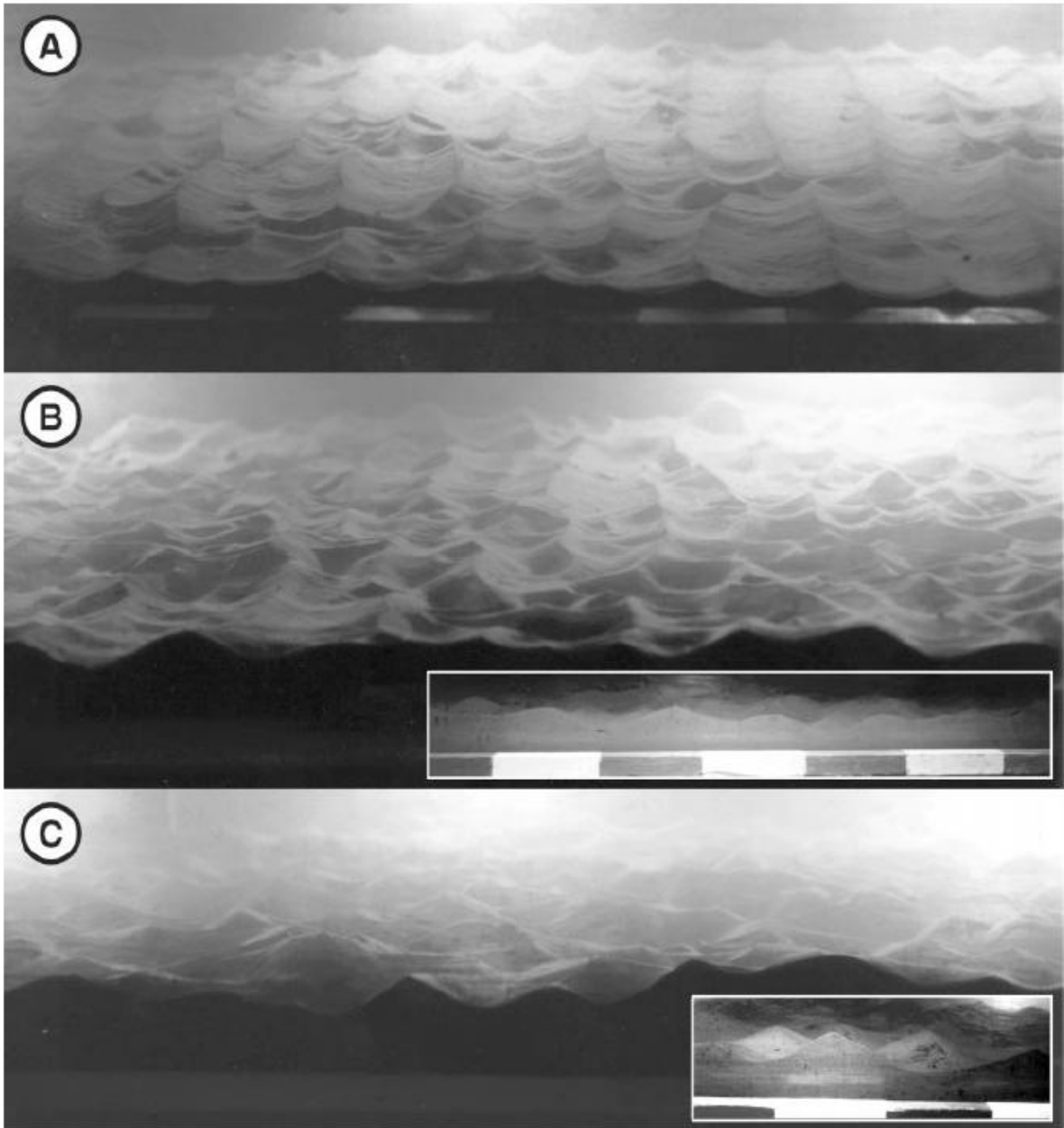


Figure 4: Small-scale ripples made in a flume, scale bars represent 0.1 m: A) Oscillatory flow ripples ($U_o = 20.1$ cm/s, $U_o = 0$ cm/s), 2D; B) Combined flow ripples ($U_o = 20.6$ cm/s, $U_o = 10.9$ cm/s), 2.5D; C) Combined flow ripples ($U_o = 20.6$ cm/s, $U_o = 21.5$ cm/s), 3D (Dumas et al., 2005).

2.2 Generic bedform classification

Stable phase diagrams

A goal of studies on bedforms in the past decades was to link the equilibrium profiles of bedforms (and other stable bed phases) to specific hydrodynamic regimes. The basic idea behind this classification is that the morphology of the bedforms depends on the flow (depth, velocity, streampower) and the sediment transport rate and mode, which depends partly on the bed characteristics. The stable phase diagrams are developed for two purposes (Kleinhans, 2005):

1. to determine the stable bed states for given flow conditions, and the other way around: modelling of near-shore flow and morphological evolution from given initial bed profiles;
2. to reconstruct paleaeo-flow conditions from sedimentary deposits.

In addition to this, the diagrams deliver insight into the effect of changing boundary conditions on bed states. On the other hand, the diagrams do not provide detailed information about the dimensions of the expected bedforms. For this goal bedform predictors were developed, these will be discussed later. The different processes that act under unidirectional, oscillatory, and combined flow have resulted in quite different phase diagrams. The development of these diagrams will be discussed below.

Phase diagrams for currents

Stable bed phase diagrams for currents are among the most detailed and verified existing phase diagrams. A vast amount of laboratory and field data has been used to derive empirical relations that define the transition between stability fields. The first diagrams were based on the grain size and some flow parameter (Simon and Richardson, 1965; Allen, 1984). Southard and Boguchwal (1990) defined the stability fields as a function of non-dimensional parameters for grain size, flow velocity, and shear stress. Van den Berg and Van Gelder (1993) introduced a bedform stability diagram based on a non-dimensional grain size (D_*), and a non-dimensional mobility parameter (θ' , the grain-related Shields parameter), following Van Rijn (1984). At present, this diagram is the standard for stable bed phases under unidirectional flow (Figure 5). Extensions of the diagram have been made later on (Van den Berg and Van Gelder, 1998; Carling, 1999), yet the basic idea remained the same. The non-dimensional grain size is calculated as

$$D^* = D_{50} \left(\frac{Rg}{\nu^2} \right)^{1/3} \quad (4)$$

where D_{50} = median grain size, $R = \frac{(\rho_s - \rho)}{\rho}$ with ρ_s and ρ the density for sediment and water, respectively, g is the gravitational acceleration, and ν is the kinematic viscosity. The grain-related current Shield parameter follows from:

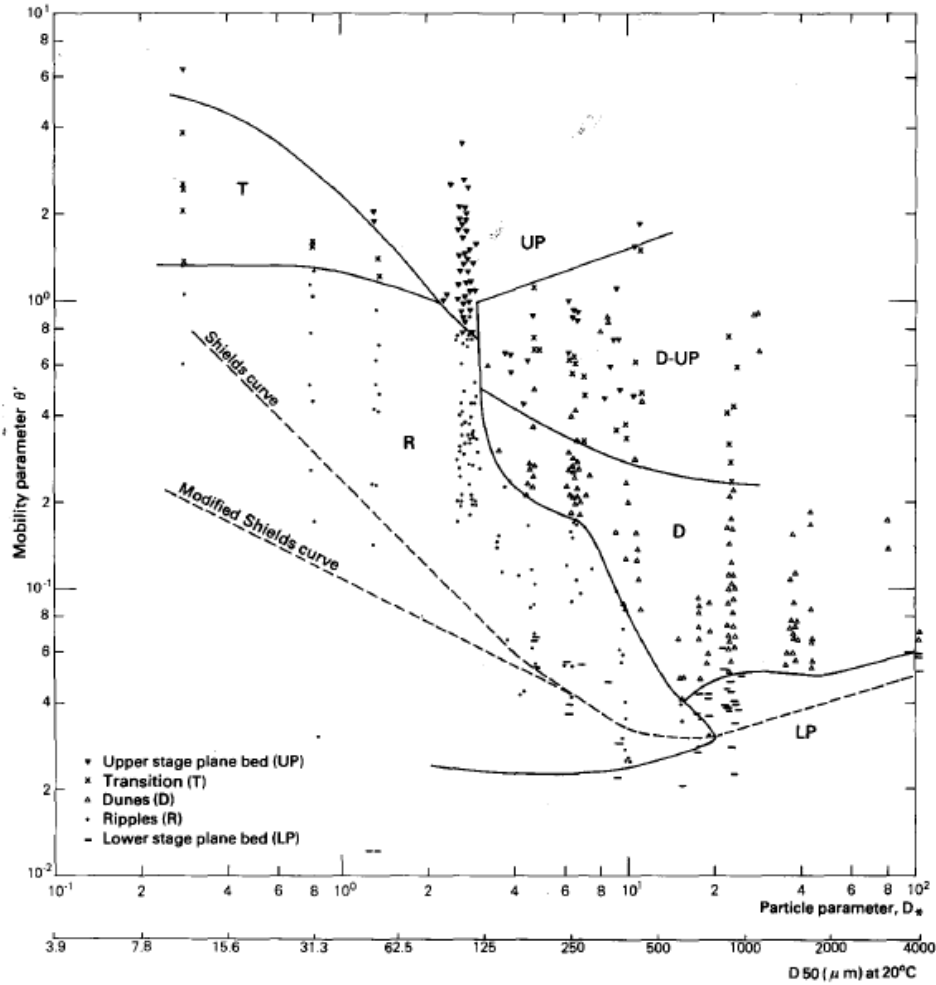


Figure 5: Stable bed phase diagram for currents (Van den Berg and Van Gelder, 1993)

$$\theta'_c = \frac{\tau'_c}{(\rho_s - \rho)gD_{50}} \quad (5)$$

Here, τ'_c is the effective shear stress induced by a unidirectional flow. Inserting the White-Colebrook friction law for hydraulic rough conditions, the shear stress is given by:

$$\tau'_c = \left(\frac{1}{8}\right) \rho f_c u^2 \quad (6)$$

with f_c the friction factor under currents:

$$f_c = 0.24 * \left[\log \left(\frac{12h}{k_s} \right)^{-2} \right] \quad (7)$$

where h is the waterdepth and k_s is the Nikuradse roughness length which follows from (Van Rijn, 1984):

$$k_s = 2.5D_{50} \quad (8)$$

In Figure 5 incipient motion is given by the Shield's curve, which was empirically derived to form a band curve which marks the region between sporadic movement and full movement. A second, modified, Shield's curve is drawn because Miller et al. (1977) found that the original curve overestimates the threshold values for silt and fine sand. The transition to Upper Plane Bed (UPB) is empirically derived for silt and fine sands and is, for the transition of dunes to UPB, described by (Van den Berg and Van Gelder, 1993):

$$\theta' = 0.69D_*^{0.34} \quad (9)$$

The transition from ripples to dunes is distinguished by the hydraulic rough/smooth boundary. The other transition lines were derived empirically. Although this diagram has shown to work well for currents over a movable bed, the diagram does not account for oscillatory flow under waves. Other diagrams have been developed for this purpose, these are discussed next.

Phase diagrams for waves

Far less stable bed phase diagrams exist for waves than there are for currents. Instead, the behavior of bed states under waves is described by empirical predictors in coastal engineering literature (Kleinhans, 2005). The best known diagram is that of Allen (1984), which is based on grain size (D) and the maximum orbital velocity (U_{max}). Another wave bed state diagram, that was presented by Kleinhans (2005), is shown in Figure 6. The diagram is, like the current bed state diagram, based on a non-dimensional grain size and a grain-related Shield's parameter. The grain-related wave Shield's parameter is modified by use of the effective wave shear stress parameter (Nielsen, 1981):

$$\tau'_w = \frac{1}{2}f_w\rho U_{max}^2 \quad (10)$$

where the wave friction factor is given by (Soulsby, 1997):

$$f_w = \exp \left[5.213 \left(\frac{2.5D_{50}}{A_{orb}} \right)^{0.194} - 5.977 \right] \quad (11)$$

Here A_{orb} represents the distance a water particle moves during one cycle. The orbital diameter is calculated as

$$A_{orb} = \frac{u_{orb} * T}{2\pi} \quad (12)$$

where u_{orb} is the orbital velocity and T is the wave period. In this wave bed state diagram the threshold for the initiation of motion ($D < 2$ mm) is given by a modification of the Shield's criterion, described by Zanke (2003). The modified Zanke model is approximated for its standard angle of repose (30°), turbulent conditions and a large ratio of water depth and grainsize (Kleinhans, 2005):

$$\theta'_{cr} = 0.5[0.145D^{*-0.5} + 0.045 * 10^X] \quad (13)$$

where X is calculated as

$$X = -1100D^{*(-9/4)} \quad (14)$$

The transition to UPB (sheetflow criterion) is described by a modification of the Allen-Leeder model (Kleinhans, 2005):

$$\theta'_{sh} = KC_0 \tan\psi \quad (15)$$

where C_0 is the bed surface sediment concentration and attains a value of 0.6, $\tan\psi$ is the angle of repose, which is 0.95 for $D < 0.2$ mm and 0.52 for $D > 2$ mm. The parameter K is a factor to account for cohesive effects in the water-sand system (assuming the sand consists mainly of quartz):

$$K = 1 + \frac{3*10^{-8}}{(\rho_s - \rho)D^2} \quad (16)$$

It should be noted that there are many studies devoted at roughness, and consequently there are many formulations for the friction factors (f_c and f_w). The choice of the friction factor can have quite different results. The friction factors are developed under different conditions and so, one need to keep in mind for what purpose the factor was originally developed.

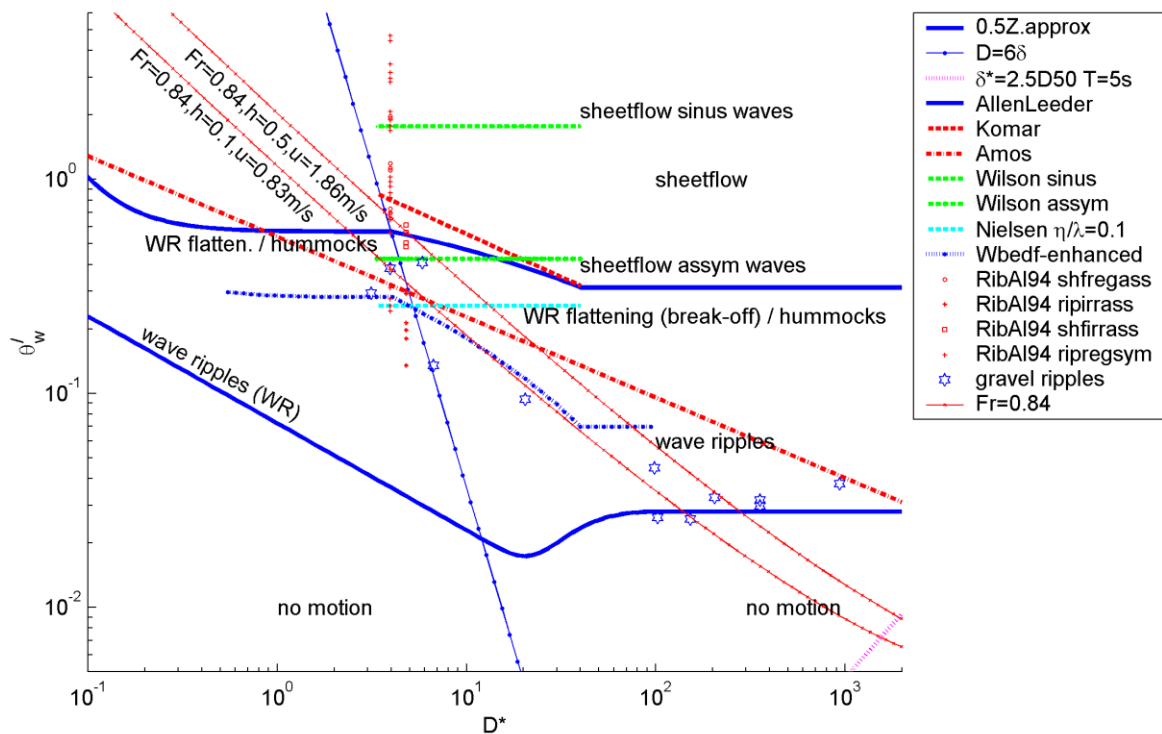


Figure 6: Stable bed phase diagram for waves (Kleinhans, 2005). The modified Zanke and Allen-Leeder criteria are given by (13) and (15), respectively. The transition from hydraulic smooth to rough conditions is given by $D=6\delta$, where δ is the thickness of the wave boundary layer. The Komar and Amos lines indicate their values for sheetflow and the Wilson data shows the effect of wave asymmetry on the sheetflow-boundary, which was tested on the Ribberink and Al-Salem (1994) data. The $Fr=0.84$ give critical flow for two waterdepth-velocity combinations.

Phase diagrams for combined flows

The combined flow stable bed phase diagrams that are available from the literature are more abundant than wave phase diagrams but not as numerous as current phase diagrams. Amos et al. (1988) were the first that presented a phase diagram for combined flow ripples (Figure 7). In Figure 7 good segregation of the bed states was found for well-developed ripples, poorly developed ripples, and flat bed by making use of the current Shield's parameter (after Sternberg, 1972) on the abscissa and the wave Shield's parameter on the ordinate (after Grant and Madsen, 1979). The diagram further distinguishes five ripple stability fields on the basis of genetics. These are wave ripples (W), wave ripples with subordinate current ripples (Wc), combined flow ripples (WC), current ripples with subordinate wave ripples (Cw), and current ripples (C). Their measurements of bedforms on the Canadian continental shelf of 20-50 m depth and waves and currents generally orthogonal were classified into eight bed states, described earlier, and showed to plot reasonable well in the diagram.

Other studies presented diagrams to segregate bed states by the strength of the unidirectional and oscillatory components (Arnoth and Southard, 1990; Yokokawa, 1995; Li and Amos, 1996). Figure 8 shows such a diagram that is based on data acquired with 0.9 mm median grain size and a wave period of 8.5 seconds. The oscillatory flow tunnel data on bed states was divided into: no movement,

small 2D ripples, small 3D ripples, large 3D ripples, and plane bed. These bed states were well separated in the diagram.

The diagram presented by Van Rijn (1993) is based on that of Amos et al. (1988), but laboratory data is additionally implemented. Here, a distinction is made between following, perpendicular, and opposing currents, which might be important as for following currents sheetflow is attained at smaller wave Shield's numbers (Ribberink, 1995). Kleinhans (2005) compared the combined flow bed phase diagrams and presented a new diagram. Because the criteria vary with grain size, the diagrams can only be plotted for one average grain size. This problem was overcome by defining a mobility parameter M , which is described by:

$$M = \left[\frac{\theta'_i - \theta'_{cr}}{\theta'_{sh} - \theta'_{cr}} \right] (\beta - \alpha) + \alpha \quad (17)$$

where θ'_i is the Shields parameter of an observation, θ'_{cr} is the value of the Shields parameter defined by the Zanke (2003) model, θ'_{sh} is the value of the Shields parameter defined by the Allen-Leeder criterion for the initiation of Upper Stage Plane bed, and the parameters α and β attain a value of 0.05 and 1, respectively. The diagram is shown in Figure 9. Initiation of motion is given by (13) and the transition to UPB by (15). Furthermore, four ripple stability fields are defined by ratios of the wave and current Shield's values. Wave only (or current only) ripples are considered as special cases where the influence of the currents (or waves) is equal to zero. Consequently, ripples that are formed solely by wave (current) action would plot in the left (lower) center part of the diagram. A certain threshold value must be exceeded before the ripples show features of the currents (or waves). The 1:1 line in the diagram separates the wave ripples with influence from currents (Wc) with current ripples with influence from waves (Cw). There is no clear stability field for mixed bedforms (WC), because it is hard, or not possible, to separate these bedforms as pure mixed bedforms. However, bedforms that are formed by the combined action of waves and currents should plot near the line of equality.

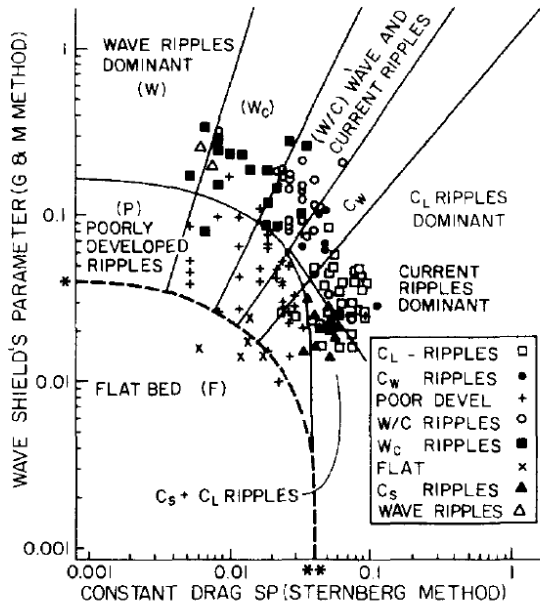


Figure 7: Combined flow stable phase diagram, based on the current and wave Shield's parameter (Amos et al., 1988)

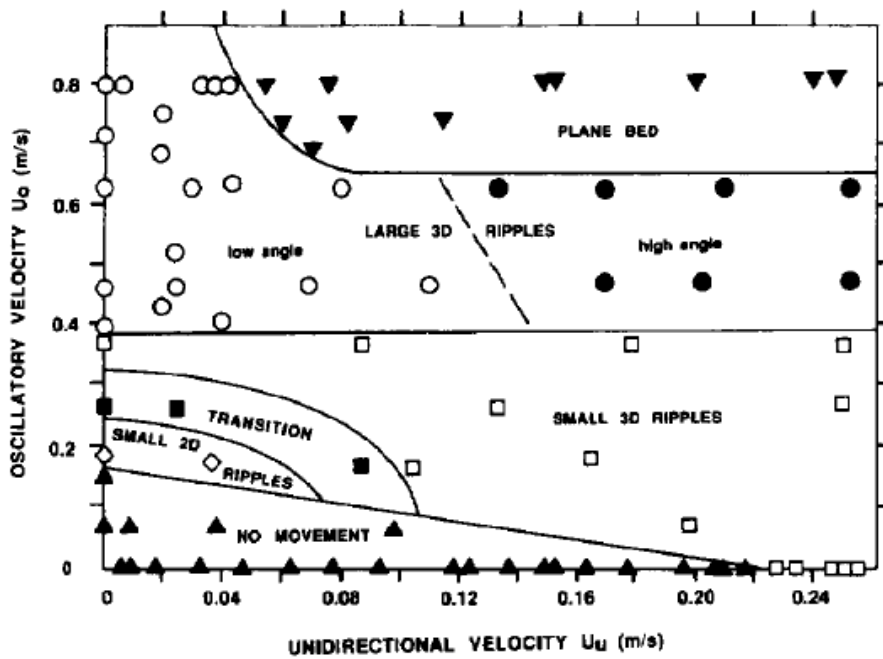


Figure 8: Combined flow stable phase diagram based on the unidirectional and oscillatory velocity components (Arnott and Southard, 1990)

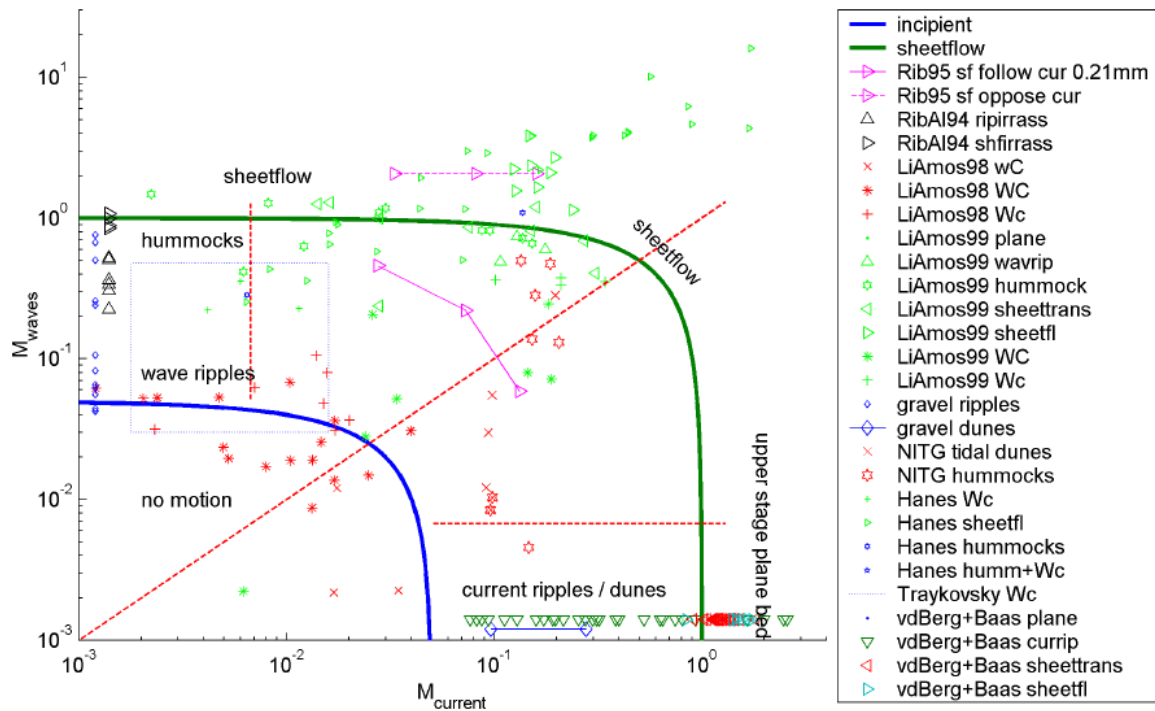


Figure 9: Combined flow stable phase diagram based on the current and wave Shields parameters. With the Zanke criterion for incipient motion (blue line) and the Allen-Leeder criterion for the transition to sheetflow (green line), see text for further explanation (Kleinhans, 2005).

2.3 Bedform dynamics

Bedform dynamics signifies the change in ripple properties (e.g. size, shape, orientation, as described in Section 2.1) with changing forcing factors. This change in forcing factor can be a change in source, direction, or relative strength of the sources. The studies to these phenomena have a highly empirical character because they are far from well understood. The empirical diagrams described in the previous chapter have had a major contribution in understanding the dynamics of the various bed states and in particular the transition from one to another bed state. A qualitative description of the development phases of ripples for varying flow conditions is given first. Thereafter, scaling relationships between bedform geometry and flow and sediment characteristics are evaluated to give a quantitative assessment on the change of dimensions with changing flow and sediment parameters.

2.3.1 Ripple ‘life cycles’

The generation, development, and destruction of current ripples is divided in four distinct stages (Baas, 1994). The flow velocity affects the rate of change of the ripples but not the development characteristics of the different stages. When the shear stress increases above the threshold value for incipient motion stage 1 is initiated (Fig. 10a). During this stage, grains move in longitudinal patches and form incipient ripples. Erosion of the sediment surface, and of juvenile ripple troughs, gradually converges the incipient ripples in straight and sinuous ripple trains, this is stage 2 (Fig. 10b).

Subsequently, the straight and sinuous ripples evolve in non-equilibrium linguoid ripple trains (stage 3) and as the flow remains, the ripples reach their equilibrium linguoid profile (stage 4, Fig. 10c). When the flow velocity increases further Upper Plane Bed (UPB) will be reached and the ripples will be washed out. During these stages the height and wavelength of the ripples evolves gradually. The height develops from zero to a maximum and breaks off towards zero again. The maximum height value and life span is not equal for every ripple. The main reason for this is the influence of adjacent ripples that shelter downstream ripples. The equilibrium ripple height and wavelengths do also not attain a specific value but fluctuate around long term averages. This is caused by the changing geometry of individual ripples at equilibrium conditions and by the three-dimensional form of ripples.

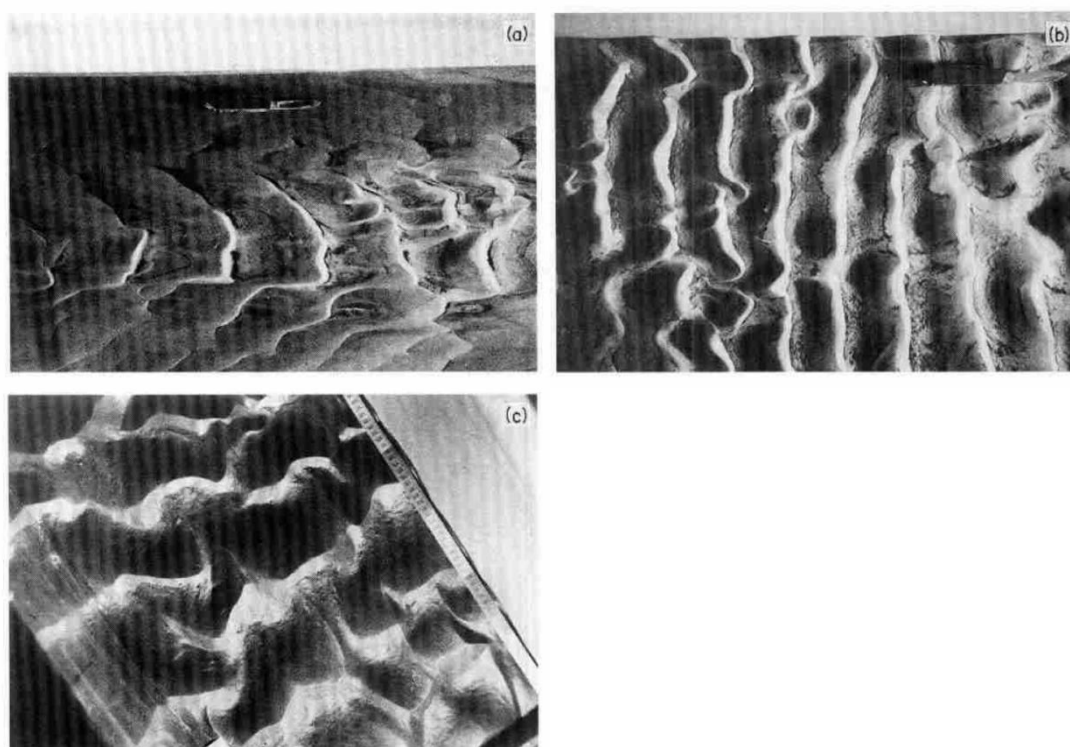


Figure 10: Photographs of current ripples in different development stages: (a) stage 1; (b) stage 2; and (c) stage 4. (Baas, 1994)

The development of bedforms under waves can be subdivided in two distinct phases. In the first phase, the equilibrium range, the bedform length scales with the near-bed orbital diameter (d_o) and bedform steepness remains approximately constant (Tanaka and Shuto, 1984). These are the orbital ripples. When the wave-orbital motion becomes stronger and bed shear stress increases beyond the equilibrium range, the ripple height will first reach a maximum and will then enter the break-off range. During this stage the size of the ripples will not increase any further with increasing stress, instead ripple height will decrease fast with increasing bed shear stress during this break-off range. A consequence is that bedform length and wave-orbital diameter do not scale anymore in the break-off range (Swales et al., 2005). These wave bedforms are called anorbital ripples. If the grain size of the

sediment is large ($D > 300 \sim 400 \mu\text{m}$) the ripples do not enter the anorbital regime but will also scale with the orbital diameter when d_o attains larger values. When bed stress increases even further the bedforms are washed out and UPB will be reached. The onset of sheet flow under waves occurs at $\theta'_w \approx 0.8$ (Soulsby, 1998). The onset of the sheet flow criterion will be reached at smaller wave Shields parameter values for increasing grain size and if a current is superimposed on the wave-orbital motion (Li and Amos, 1999).

The generation, development, and destruction of ripples induced by combined flows is less understood than the development phases of wave or current ripples. The ratios of the skin-friction wave to current shear velocity can be used to separate combined flow, wave-dominant, and current-dominant (Li and Amos, 1996; Section 2.2.3). However, the ratio of these components is not the only factor that determines ripple type. The morphology is complicated because the wave ripple threshold is influenced by the currents, and the current ripple threshold is influenced by the waves. The final ripple morphology is defined by the partitioned, wave and current components of stress and not by the total stress (Amos et al., 1988). Examining the partitioned effect of the currents and waves on combined flow ripple morphology is the essence of understanding combined flow bedform dynamics.

Effect of oscillatory flows

Under a pure unidirectional flow the ripples have an asymmetric linguoid profile with round crests. The addition of an increasing oscillatory flow on a small unidirectional flow under an angle of 0 or 180° ($\leq 10 \text{ cm/s}$) causes the ripple morphology to evolve from small-scale, symmetric, anorbital ripples towards large-scale, symmetric, orbital ripples (Dumas et al., 2005). A similar development is observed under larger unidirectional velocities but the ripples are more asymmetric. This can be explained by Figure 8, the larger relative strength of the unidirectional flow makes the ripples current-dominant and so, more asymmetric.

Effect of unidirectional flows

The effect of the addition of a following or opposing increasing unidirectional flow on an oscillatory flow is that the ripple becomes more asymmetric. The lee and stoss sides become convex-upward and the overall shape becomes rounded. Furthermore, the crestlines become more discontinuous and the bedforms become increasingly three-dimensional. The bedforms will be 3D at $U_u \sim 10\text{-}15 \text{ cm/s}$ for small-scale ripples and at $U_u \sim 13\text{-}18 \text{ cm/s}$ for large-scale ripples (Bridge and Best, 1988). This can be seen in Figure 8, for low oscillatory velocities the bedforms gradually evolve from small 2D ripples to small 3D ripples under an increasing current. The direction of the current, with the direction of wave propagation (following) or against it (opposing), does not influence the successive changes in ripple profile. The only effect is that ripples become more asymmetric under following than under opposing currents. This is caused by the fact that there is a relatively strong (wave-induced) reduction of the near-bed current velocities in the case of an opposing current (Van Rijn, 1993). Wavelength and

height are also not noticeably effected by currents that act under an angle (60°, 90°, 120°) (Van Rijn, 1993). The morphology, on the other hand, is influenced by the direction of the current. When the current is perpendicular to the direction of the waves the ripples will develop a serpentine crestline pattern (Young and Sleath, 1990).

Effect of grain size

Yokokawa (1995) found that the wavelengths of medium sand (0.29 mm) combined flow ripples were 2.5 times larger than for ripples formed under similar conditions with fine sands (0.18 mm), and that smaller grain sizes (course silts, 0.06 mm) yield a wavelength of 0.9 times the length found in medium sands. Furthermore, it was found that the height of the ripples increases with grain size but that the profiles of the bedforms were very similar. This observation does not agree to the findings of Dumas et al. (2005) and Southard et al. (1990) who found in their laboratory runs better developed three-dimensional profiles for combined flow ripples and oscillatory ripples using a finer grain size (see Section 2.1).

2.3.2 Response time and hysteresis

Bedforms are continuously adjusting their size and shape to the instantaneous flow conditions. Because the hydrodynamic conditions change on a far smaller timescale than that the bedforms can adapt, this implies that the bedforms are never in equilibrium. The time that it takes for bedforms to adapt to the prevailing conditions is shorter for small-scale bedforms than for large-scale bedforms. This is because the rate of change depends on the magnitude of sediment transport, and larger bedforms have a larger volume of sand that has to be reworked (Kleinhans, 2005). Very large-scale bedforms may even not adapt at all but become relict features because the bedforms are formed in a high energetic regime and are not broken down in a lower energetic regime. A good example is the preservation of hummocks during falling tide or waning storm (Kleinhans, 2005). For bedform geometry predictors this means that bedform geometry may not only be a function of the present hydrodynamic conditions and sediment properties but also on the former conditions.

Doucette and O'Donoghue (2006) performed full-scale laboratory experiments on the adaptation of sand ripples that formed under oscillatory flow. They showed that the number of flow cycles, which is the ratio of the flow period (i.e. wave period) to the time to reach equilibrium, to reach equilibrium geometry is related to the mobility number ψ (Fig. 11). The number of flow cycles showed an exponential decrease with the mobility number, described by:

$$n_e = \frac{t_e}{T} = \exp(-0.036\psi + 7.44) \quad (18)$$

Here n_e represents the number of flow cycles, t_e is the time to reach equilibrium, and ψ is the mobility parameter. Although this relation was based on experiments using one sand size only ($d_{50} = 0.44$ mm) it can be reasoned that n_e also depends on the grain size diameter because this is an important parameter determining the mobility parameter. The time to reach equilibrium geometry was not dependent on the initial bed morphology. This implies that when the equilibrium and initial bed morphologies are more unlike, the rate of change needs to be higher in order to reach equilibrium in the same amount of time.

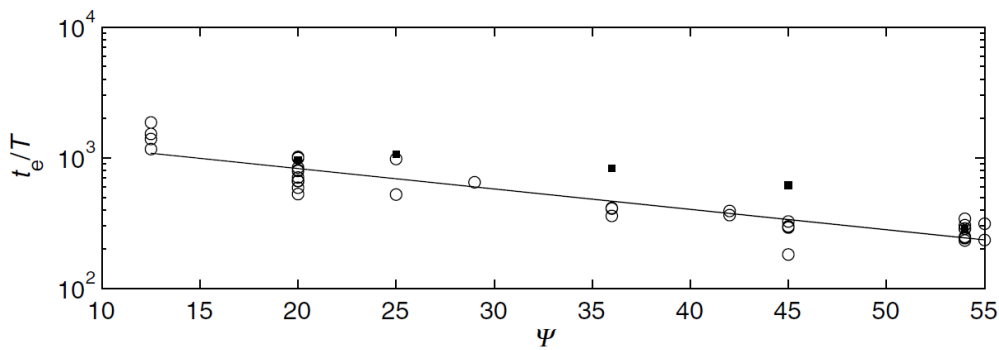


Figure 11: Number of flow cycles and mobility number for oscillatory sand ripples in a laboratory setting.

A field study on an intertidal beach showed that wave-induced ripples are strongly influenced by relaxation time effects (Austin et al., 2007). Ripple wavelength and height were observed to progressively increase during the rising tide but remained constant during the falling tide, the ripples were not altered by the waning energy conditions (Fig. 12a and b). Thus, during the ebb stage the relaxation time of the bedforms caused hysteresis, as the change in ripple geometry lags behind on the hydrodynamic forcing. These observations clearly depict that the tide modulates the hydrodynamic conditions at a far higher rate of change than the relaxation time of the ebb ripples. This suggests that, in contrast to the observations of Doucette and O'Donoghue (2006) where hydrodynamic conditions were long enough constant for the ripples to reach equilibrium, the instantaneous bed morphology is, in fact, dependent on the initial bed morphology. This dis-equilibrium situation during the falling tide can have significant implications for suspended sediment transport processes. The over-developed ripples during the falling tide cause a larger roughness and can possibly enhance sediment suspension (Austin et al., 2007).

Soulsby et al. (2012) discuss the implication of this relaxation time effect for ripple geometry predictors. They argue that predicting the rate of response of the ripples is just as important as the equilibrium geometry. The approach they used for the time-evolution of ripples in their ripple geometry predictors will be discussed later on in Section 2.4.

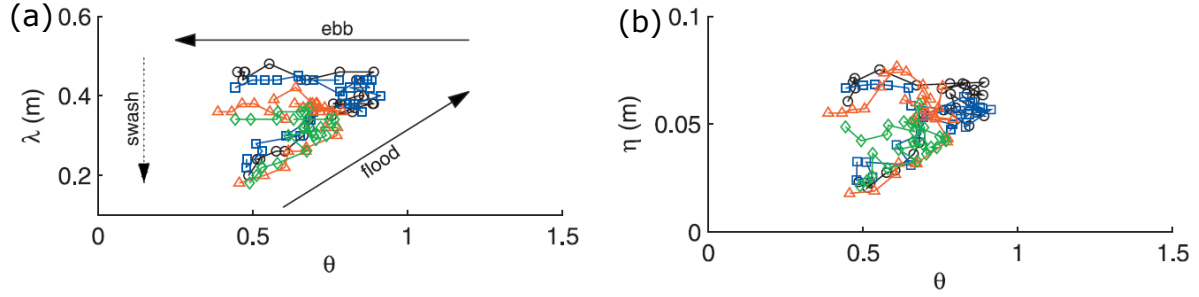


Figure 12: (a) Evolution of ripple length, and (b) evolution of ripple height as function of non-dimensional wave Shields number. The colors and symbols denote different tidal cycles. (Austin et al., 2007)

2.4 Modelling bedform geometry

2.4.1 Scaling relationships

The dimensions of bedforms depend on the flow and sediment characteristics. Consequently, there must be a relation between the geometry of the bedforms and one, or more, flow and/or sediment parameters. Finding these scaling relationships is the key element for predicting bedform geometry based on the flow and sediment characteristics. In this section first the scaling relationship of wave-induced ripples will be discussed and it will be explained why combined flow ripples do not scale to the same parameters. Thereafter, scaling relationships of combined flow ripples will be presented.

Scaling wave ripple geometry

Wave ripples have been classified into three different classes, based on the scaling relationship of the ripple wavelength λ (Clifton, 1976). Orbital ripples are wave ripples where λ scales with the horizontal excursion length d_o , these ripples are found at small values of the ratio of the wave orbital diameter to mean grain diameter ($\frac{d_o}{D} < 1 \times 10^3$). Anorbital ripples are wave ripples that do not scale with d_o but show a relationship with the grain size. Anorbital ripples are found at larger values of this ratio ($\frac{d_o}{D} > 1 \times 10^5$). At intermediate wave energy conditions there is a transitional range of d_o/D values, with intermediate wavelengths. The ripples formed in this transitional range are called suborbital ($1 \times 10^3 < \frac{d_o}{D} < 1 \times 10^5$). These scaling regimes are shown in the Clifton and Dingler (1984) classification scheme for wave-formed ripples (Fig. 13a). Here, the boundaries between orbital, sub-orbital, and anorbital ripples are indicated by the dashed lines. Furthermore, a segregation of coastal bedforms was made by the bedform height to length ratio, the steepness (Fig. 13b). Here, $\eta/\lambda > 0.15$ was classified as vortex ripples, pointing at the vortex of sediment plumes that exist on the lee sides of the ripples. Below this threshold the ripples were described as post-vortex ripples.

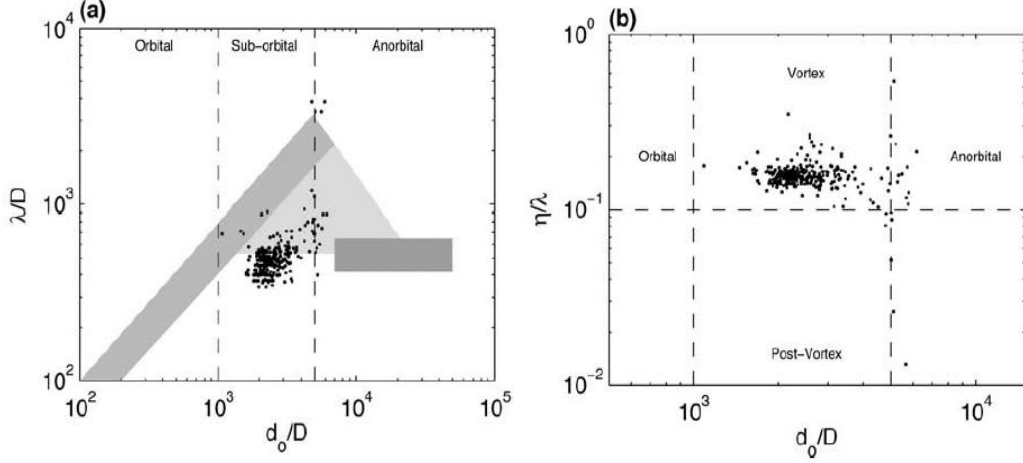


Figure 13: Ripple classification schemes of Clifton and Dingler (1984). (a) Differentiation between orbital, sub-orbital, and anorbital ripples by their scaling with d_0 and D . (b) Differentiation between vortex and post-vortex ripples by their steepness (from Masselink et al., 2007)

Figure 14a shows the non-dimensional wavelength (λ/D) for orbital ripples that are generated by purely oscillatory flow, plotted versus the non-dimensional horizontal excursion distance (d_0/D). The data in the figure is obtained from wave flume and oscillatory water tunnel experiments. The figure confirms that the length of wave-induced sand ripples in the equilibrium region is proportional to the horizontal excursion length of the water particles near the bottom. The relation is described by

$$\frac{\lambda_{orb}}{D} = 0.65 \frac{d_0}{D} \quad (19)$$

where the horizontal excursion distance is given by

$$d_0 = \frac{\hat{U}_w T}{\pi} = \frac{HT}{L} \frac{\frac{L}{T} \pm \bar{u}_0}{\sinh \frac{2\pi h}{L}} \quad (20)$$

Here, H is the wave height, \hat{U}_w is the amplitude of the horizontal velocity of the oscillatory flow, just outside the boundary layer, \bar{u}_0 is the vertically averaged velocity of the unidirectional flow, which is zero in this case of purely wave motion. L represents the wavelength (of the waves) and is calculated by the following dispersion relationship:

$$\left(\frac{L}{T} \pm \bar{u}_0\right)^2 = \frac{gL}{2\pi} \tanh\left(\frac{2\pi h}{L}\right) \quad (21)$$

Here the sign is taken negative and positive for a following and opposing current, respectively. Figure 14b shows ripple steepness plotted versus the maximum Shields number. It indicates that ripple

steepness remains approximately constant as the non-dimensional shear stress (Shields number) is less than 0.2. The relation of ripple steepness to non-dimensional shear stress is described by

$$\frac{\eta}{\lambda} = 0.25\sqrt{0.6 - \theta'_w}, \text{ for } \theta'_w < 0.6 \quad (22)$$

Anorbital ripples do not show a clear relation with the hydrodynamic conditions, however, the ripple wavelength of anorbital ripples is found to scale with a multiple of the grain diameter. One relation that scales anorbital ripples to grain diameter is described by Clifton and Dingler (1984) as:

$$\lambda_{ano} \approx 500D \quad (23)$$

The maximum steepness of anorbital ripples is smaller than for orbital ripples, approximately 0.12, and decreases for increasing wave conditions. The steepness decreases until sheetflow conditions are reached (Wiberg and Harris, 1994).

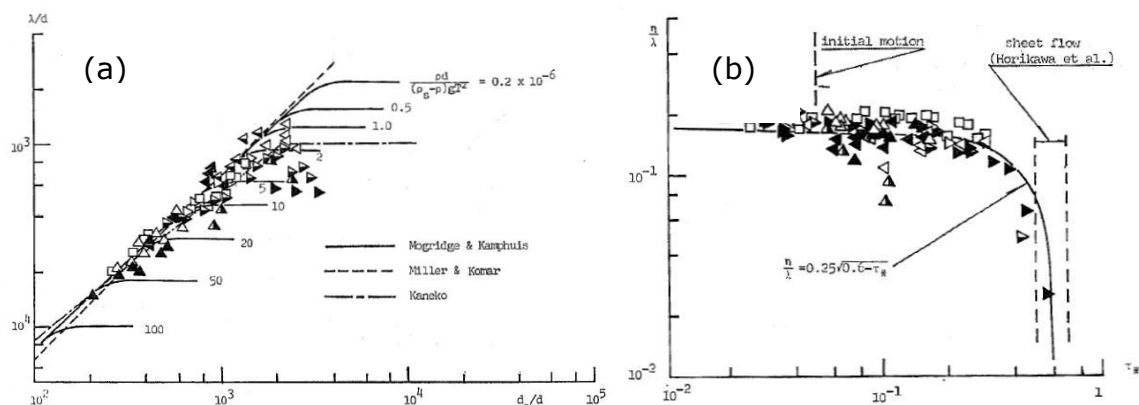


Figure 14: a) Variation of λ/D with d_o/D for oscillatory flow data. b) variation of η/λ with τ_* for oscillatory ripple data (Tanaka and Shuto, 1984).

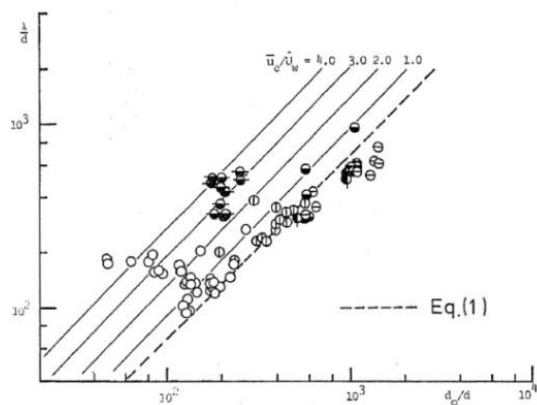


Figure 15: Non-dimensional wave-current bedform wavelength versus non-dimensional horizontal excursion length. Oblique lines represent ratios of steady and oscillatory velocities. Dashed line represents equation 19. (Tanaka and Shuto, 1984).

Scaling combined flow ripple geometry

The geometry of ripples that are formed by the combined action of waves and currents must depend on both the oscillatory and unidirectional components of the flow. Figure 15 shows the non-dimensional wavelength (λ/D) for combined flow (angle between waves and currents 180°) ripples plotted against the non-dimensional horizontal excursion distance. The dashed line in the figure represents equation 19, the relation that correctly describes wavelength for orbital ripples. The solid lines represent the equivalence lines concerning \bar{u}_0/\hat{U}_w . The data points that plot left from equation 19 are measurements where the steady component was more dominant. It can be seen that when the unidirectional component of the combined flow becomes more important, the geometry of the ripples is not described adequately by (19) anymore. The data points tend to shift to the left in the diagram, meaning that ripples with a certain wavelength will be produced under lower energetic wave conditions (smaller d_0) when a current is super imposed. Apparently, the wavelength of combined flow ripples does not scale solely to d_0 anymore when the unidirectional flow becomes dominant over the oscillatory component.

That the ripple wavelength does not scale to the oscillatory excursion distance anymore is caused by the influence of the current. A smaller value of d_0 is already sufficient to produce a ripple of equal length when a current is superimposed, this smaller value is called $d_0^{(2)}$. The difference between the horizontal excursion distance under waves (called $d_0^{(1)}$) and $d_0^{(2)}$ represents the effect of the current, this difference is labelled α (Tanaka and Shuto, 1984). Thus, the non-dimensional wavelength of combined flow ripples is not only a function of the horizontal excursion distance anymore but also on α . This property ($d_0 \cdot \alpha$) is further referred to as the 'equivalent orbital length'. Figure 16 shows a plot of the non-dimensional ripple wavelength and the equivalent orbital length. The data collapses far better when compared to Figure 15.

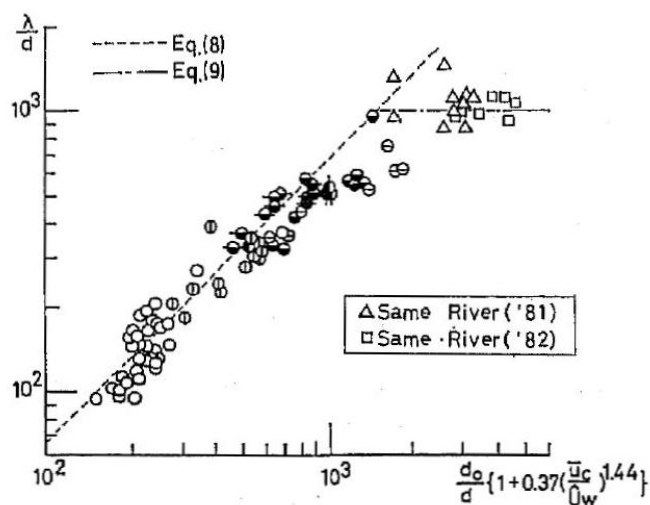


Figure 16: Dependence of non-dimensional combined flow ripple wavelength to $\frac{d_0}{d}$ times α (the part between brackets) (Tanaka and Shuto, 1984).

Refinement of the above relationship was proposed by the use of d_w (= fluid-orbit diameter at the edge of the boundary layer) and U_δ (= velocity amplitude at the edge of the boundary layer), instead of d_0 and U_0 (Tanaka and Dang, 1996). It was shown that the wavelength is a function of the ratio \bar{u}/U_δ and some dimensionless sediment parameter, described by

$$S_* = \frac{D\sqrt{(s-1)gD}}{4\nu} \quad (24)$$

However, more recently it was demonstrated that the predictors based on these parameters are inadequate when the currents interact oblique or perpendicular to the waves (Khelifa and Ouellet, 2000). Furthermore, it was shown that the combined flow ripple height depends crudely on the ratio of the skin-friction combined shear velocity and the critical shear velocity (u_{*wc}/u_{*cr}) (Li and Amos, 1996).

Khelifa and Ouellet (2000) discuss that pure wave or current motion is only a special case of combined flows, and the geometry of combined flow ripples should depend on a combined length scale (d_{wc}) and a combined mobility parameter (ψ_{wc}). This combined length scale was referred to as the ‘effective fluid orbital diameter’:

$$d_{wc} = TU_{wc}^{0.5} \quad (25)$$

with U_{wc} the maximum velocity at the edge of the combined wave-current boundary layer, described by:

$$U_{wc} = \left(\frac{U_\delta}{\pi}\right)^2 + \bar{u}^2 + 2\frac{U_\delta}{\pi}\bar{u}|\cos\phi| \quad (26)$$

where U_δ is the maximum orbital velocity at the edge of the wave boundary layer, \bar{u} is the depth-averaged current velocity, and ϕ is the angle between the current and the direction of wave propagation. The combined flow mobility parameter is given by

$$\psi_{wc} = \frac{U_{wc}^2}{(s-1)gD} \quad (27)$$

Figure 17 shows that scaling the non-dimensional wavelength with (27) delivers less scatter than scaling the wavelength with α .

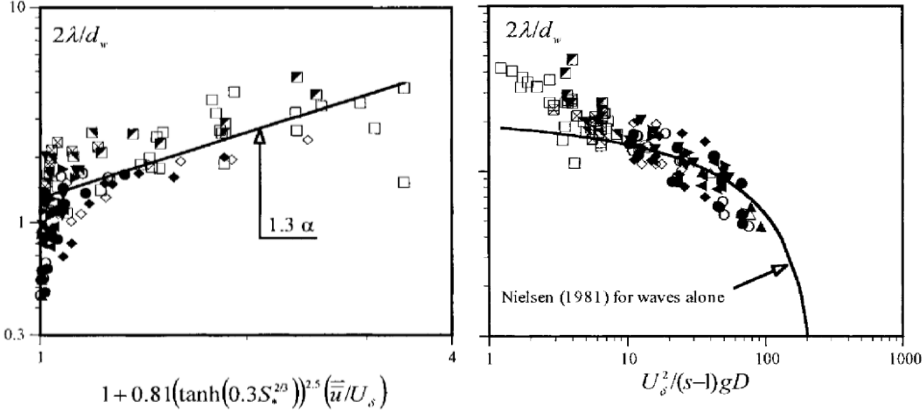


Figure 17: Plots of the non-dimensional wavelength with α (left) and ψ_{wc} (right). The solid lines represent the wavelength predictor of Nielsen (1981) (Khelifa and Ouellet, 2000).

2.4.2 Predicting combined flow bedform geometry

Predicting the dimensions of bedforms on the sea bed is highly important for determining the bed roughness felt by currents and waves and for sediment transport applications (Soulsby et al., 2012). Furthermore, it was shown that the predictions of suspended sand concentrations improve when a bedform predictor is implemented in advection diffusion equations for suspended sand concentrations (Grasmeijer and Kleinhans, 2004). Thus, the necessity of an accurate model that predicts bedforms dimensions for ripples in the nearshore zone is demanded for coastal sediment transport modeling. The available wave bedform geometry predictors are numerous and thoroughly tested. The Nielsen (1981) wave predictor [N81] is one of the most widely used predictors for wave-formed bedform geometry. The predictor is based on the wave mobility parameter ψ . This parameter is calculated the same way as equation 27 with the exception that U_{wc} is replaced with the mean peak orbital velocity ($u_{1/3}$). With this predictor, bedform height is calculated as:

$$\frac{\eta}{A} = 21\psi^{-1.85} \quad \psi > 10 \quad (28)$$

$$\frac{\eta}{A} = 0.275 - 0.022\psi^{-0.5} \quad \psi < 10 \quad (29)$$

and bedform length with

$$\frac{\lambda}{A} = \exp\left(\frac{693 - 0.37 \cdot \log^8(\psi)}{1000 - 0.75 \cdot \log^7(\psi)}\right) \quad (30)$$

Here, A is given by equation 12. Grasmeier and Kleinhans (2004) [GK04] presented a wave bedform geometry predictor that is also based on the wave mobility parameter and is a modification of the Nielsen (1981) predictor. Bedform height and length are given by this predictor by

$$\frac{\eta}{A} = 21\psi^{-1} \quad \psi > 10 \quad (31)$$

$$\frac{\eta}{A} = 0.275 - 0.022\psi^{0.5} \quad \psi < 10 \quad (32)$$

$$\frac{\eta}{\lambda} = -0.078 - 0.355\psi^{-0.221} \quad \psi > 10 \quad (33)$$

$$\frac{\eta}{\lambda} = 0.14 \quad \psi < 10 \quad (34)$$

The two wave predictors have proven to be reasonably adequate for wave-dominated environments and the [GK04] predictor is based on a dataset obtained from the same field site as is used in the present study. So it will be likely that they will also perform reasonably well for the wave formed bedforms in the present study.

The development of wave-current bedform predictors is more empirical because the non-linear interaction between waves and steady currents is yet not well understood. In general, the predictors are based on existing predictors for current alone and wave alone bedform predictors. A model that is based on a wave predictor, but is modified to fit data under wave-current conditions, is the Li et al. (1996) predictor [Li96]. This predictor is a modification of the Grand and Madsen (1982) wave predictor and is based on the maximum grain-related skin friction wave Shields parameter (θ'_{wm}). The dimensions are calculated as follows (primes are omitted for ease):

For $\theta_{wm} < \theta_B$

$$\eta = 0.101A_b \left(\frac{\theta_{wm}}{\theta_{cr}} \right)^{-0.16} \quad (35)$$

$$\lambda = 0.495\eta \left(\frac{\theta_{wm}}{\theta_{cr}} \right)^{0.04} \quad (36)$$

And for $\theta_{wm} > \theta_B$

$$\eta = 0.356A_b \left(\frac{\theta_{wm}}{\theta_{cr}} \right)^{-1.5} \quad (37)$$

$$\lambda = 3.03\eta S_*^{-0.6} \left(\frac{\theta_{wm}}{\theta_{cr}} \right) \quad (38)$$

where A_b is semi-orbital excursion diameter (equation 12) and S_* is given by equation (24), and the breakoff skin-friction Shields parameter is given by

$$\theta_B = 1.8\theta_{cr} S_*^{0.6} \quad (39)$$

Here, θ_{cr} is the critical Shields parameter as described by Soulsby (1997):

$$\theta_{cr} = \frac{0.3}{1+1.2D} + 0.055(1 - \exp(-0.02D)) \quad (40)$$

It was proved that following and opposing currents produce a similar effect on combined flow ripple length and height, i.e., their behaviour is symmetrical (Khelifa and Ouellet, 2000). For these reasons a combined length scale and mobility parameter should be used in combined flow bedform predictors. Khelifa and Ouellet (2000) developed such a predictor that is based on the a combined length scale and combined mobility parameter [KO00]. The formulation for ripple length by this new predictor is given by:

$$\frac{2\lambda}{d_{wc}} = 1.9 + 0.08 * \log^2(1 + \psi_{wc}) - 0.74 * \log(1 + \psi_{wc}) \quad (41)$$

and ripple height is given by:

$$\frac{2\eta}{d_{wc}} = 0.32 + 0.017\log^2(1 + \psi_{wc}) - 0.142\log(1 + \psi_{wc}) \quad (42)$$

where d_{wc} and ψ_{wc} are given by (25) and (27). The applicability of these predictors has been validated for ψ_{wc} varying in the range from 0.7-145.

The four bedform geometry predictors described before are developed for wave-dominant or combined flow conditions. They are, however, based on totally different parameters and the approach the problem in different ways. The [N81] and [GK04] models make use of the wave mobility parameter. This parameter has proven to be useful for wave-dominated conditions yet might lack accuracy for combined flow conditions. The [Li96] model is based on totally different parameters which can signify the importance of the chosen parameters. The [KO00] model makes use of modifications of the orbital excursion length (d_0) and wave mobility parameter (ψ) to account for the effect of super imposed currents. The model is however, in contrast to the other three, based on experimental laboratory results. This might cause a deficit of the model for field data.

3 Methods

3.1 The study site

The data presented and analysed in this thesis was collected during a field campaign that was carried out between 3 October and 1 November 2013. The measurements were collected at a field site located at the North Sea coast, approximately four kilometers south of the village of Egmond aan Zee, the Netherlands. At this field site a stationary tripod measurement frame was deployed at the intertidal stretch of the beach, approximately 50 m seaward of the dune foot (Figure 18, N 52 35.544; E 4 36.808). During the field campaign the morphology of the beach changed and as a consequence, the frame was alternately positioned on top of a sandbar, on the landward slope of a bar, on the seaward slope of a bar, or in an intertidal channel. This resulted in a full range of hydrodynamic and bed state conditions during the campaign.

The local environment at the field site is characterized by a semi-diurnal tide with a local mean tidal amplitude of approximately 1.5 – 2 m. Waves approached the shore under varying angles from 208° to 311° with respect to north (Figure 19), with a mean significant wave height of 0.39 m. Peak wave periods were in the range of 2 – 20 seconds. During the measurement campaign three storm events occurred.

The beach itself consists of non-cohesive sand, mainly quartz. The grain size of the sand was determined from daily grab samples that were collected during low tide, near the tripod frame. A still water particle fall velocity tube was used to determine the grain size distribution of every grab sample. This was done with three repetitions for every sample. The method of Van Rijn (1993), which relates particle fall velocity for natural sediment to the sieve diameter, was used to determine the median diameter of every grab sample. The relation of particle fall velocity (w_s) and sieve diameter (d) is given by

$$w_s = \frac{10\nu}{d} \left[\left(1 + \frac{0.01(s-1)gd^3}{\nu^2} \right)^{0.5} - 1 \right] \quad (43)$$

where s is the specific gravity (= 2.65) and ν is the kinematic viscosity coefficient, which is dependent on the water temperature. The temperature of the water was throughout the experiment approximately 19 °C. The distribution of the calculated median grain diameter is shown in Figure 20. The mean D50 is ~330 μm with a standard deviation of ~50 μm . This fairly large variation in median grain size is, however, mainly attributed to the grab samples collected at 6, 7, and 9 October. When these days are not taken in to account, the mean D50 is ~315 μm with a standard deviation of ~21 μm . For the processing of the hydrodynamic data a constant mean diameter of 315 μm was used for the entire length of the measurement campaign.

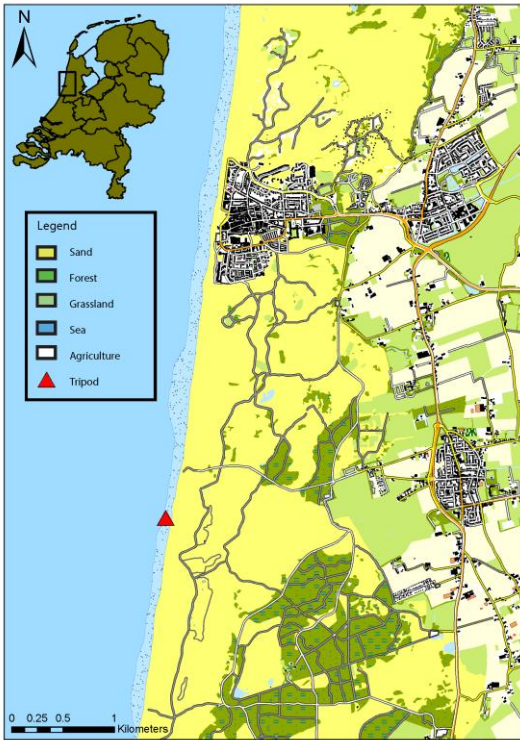


Figure 18: Overview map of the beach near Egmond aan Zee. The location of the field site is indicated by the red triangle. The light blue dotted area indicates the intertidal stretch of the beach (Source: Top10 NL).

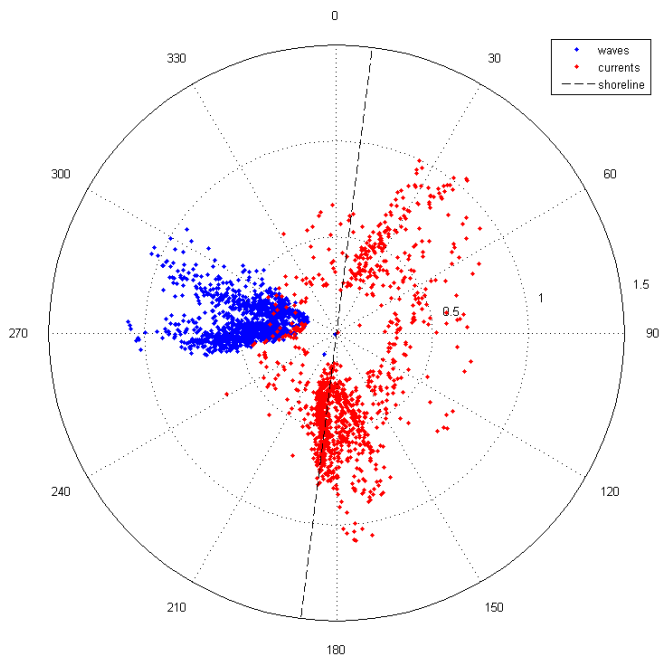


Figure 19: Wave and current rose of the measurements collected during the fieldwork. The blue dots indicate the direction where sea/swell waves were coming from and the magnitude of the waveheight (m), red dots indicate the direction where currents are coming from with current strength (m/s), and the black dashed line indicates the position of the shoreline, with the tripod in the center of the circle.

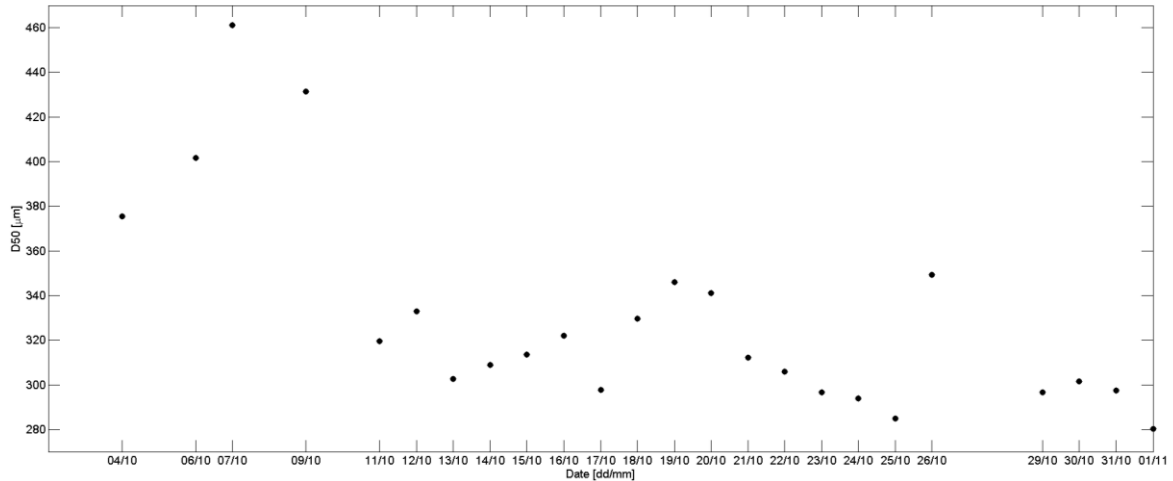


Figure 20: Median grain size (D_{50}) of grab samples collected during the field campaign. Every data point is an average of three consecutive measurements with the particle fall velocity tube.

3.2 Instrumentation

Measurements of hydrodynamics, sediment concentrations and local bathymetry were collected at the tripod frame during the entire length of the field campaign. The frame was instrumented with a pressure transducer (PT), two electromagnetic flow meters (EMFs), seven optical backscatter sensors (OBSs), a three frequency acoustic backscatter system (ABS), three acoustic Doppler velocimeters (ADVs) and a three-dimensional Sonar Ripple Profiling Sensor (3DSRPLS). A float mounted near the bed controlled the recording in 30-minute burst periods by evaluating if the frame was submerged (on) or emerged (off). The frame, with all the instruments indicated, is shown in Figure 21. In this thesis the data of PT, EMF, and 3DSRPLS will be used.

The pressure transducer sampled at a frequency of 4 Hz to record the pressure of the overlying water column. This data was corrected for atmospheric pressure which was recorded with another pressure sensor ashore. The EMFs operated, likewise the pressure transducer, with a sampling frequency of 4 Hz to measure the magnitude of the velocity components in the horizontal plane. The 3DSRPLS was mounted on the seaward side of the tripod frame. It looked downwards in order to scan the bed directly under the frame. The sonar operated at a frequency of 10 MHz and measured the backscatter intensity from 0 m to 4 m under the measuring head in 842 equally spaced bins under a swath arc of 150° with 0.9° spacing, giving 166 points with backscatter intensity, for each scan line. The scanner rotated half a circle with 0.9° increments, giving 200 scan lines. Consequently, every sonar image consists of $166 \times 200 = 33,200$ points with backscatter intensity. The diameter of the scanned surface varied during the campaign due to aggradation and erosion of the bed. The distance between bed and sonar varied between 0.48 – 0.71 m during the campaign, resulting in a scanned surface which varied between 10.08 – 22.05 m^2 . The density of data points depends on the size of the scanned surface and consequently, the spatial step size of measured points on the bed was dependent on the distance

between the measuring head and the bed. The average spatial step size varied during the campaign from $3.04 \cdot 10^{-4} \text{ m}^2$ (distance is 0.48 m) to $6.64 \cdot 10^{-4} \text{ m}^2$ (distance is 0.71 m). However, the spatial step size was smaller than the average spatial step size directly under the measuring head and decreased towards the outer rim of the scanned surface. The sonar completed one full scan in 15 minutes, giving two completed sonar images for every 30-minute burst of hydrodynamic data if the sonar was submerged.

Besides the measurements that were acquired by the tripod a series of GPS surveys were carried out to map the local morphology of the area surrounding the field site. These surveys were conducted with a quad-mounted DGPS device that sampled at an interval of 1 second (approximate average velocity 10 km/h) with an accuracy of 2.5 cm in the horizontal and 4 cm in the vertical plane.

Next to the measurements that were acquired by the frame and the GPS surveys, photographs of the surrounding area of the field site were taken from an Argus video station (Egmond, Coast3D tower). These cameras are monitoring the beach since 1998 by taking photographs every 30 minutes as part of the Coast3D project (<http://argus-public.deltares.nl/archive/>). These photographs were, together with field observations and the quad surveys, used to determine the morphological setting of the beach at specific time intervals.

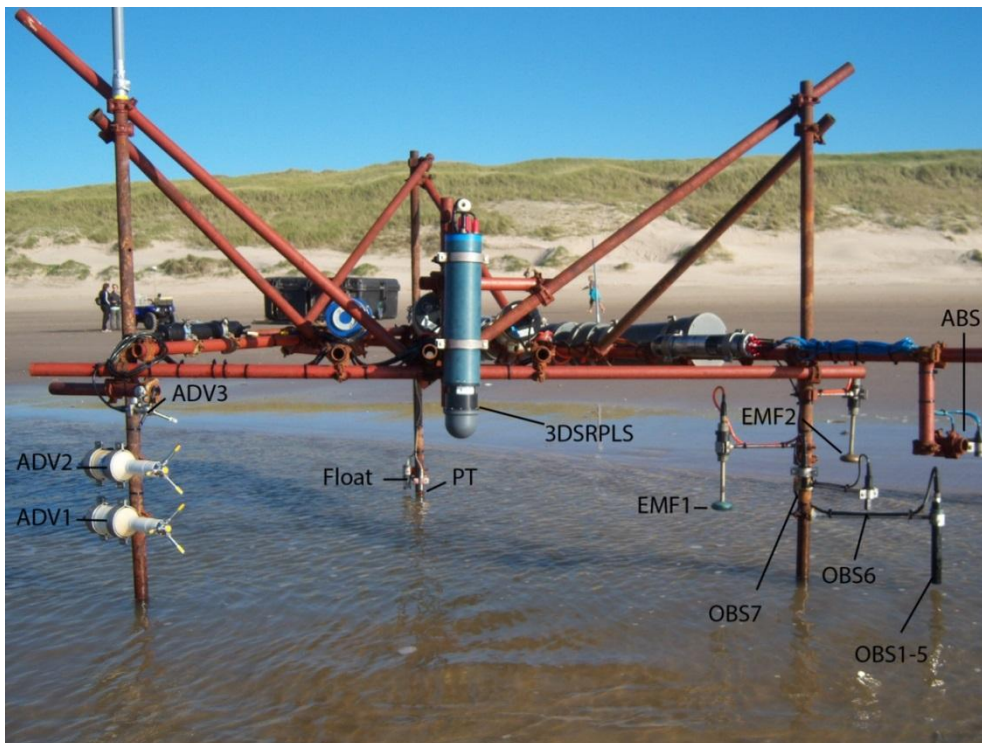


Figure 21: The stationary tripod frame, located at the low tide water line. The instruments are indicated. Orientation of the three ADVs was 210° and the positive x and y directions of the two EMFs were respectively 265° and 175° for EMF1 and 253° and 163° for EMF2. The PT is located close to the bed to acquire a long tidal measuring time span. The 3DSRPLS is mounted fairly high above the bed to scan a broad area under the sonar.

3.3 Data processing

3.3.1 Hydrodynamics

The pressure transducer collected pressure measurements which were stored in mV. The signal was calibrated to mBar after which free water surface elevation was obtained through

$$\eta_t = \frac{100p}{\rho g} \quad (44)$$

where p is the calibrated and atmospheric corrected pressure signal (mBar), ρ is the water density (1000 kg/m^3) and g is the gravitational acceleration (9.81 m/s^2). The total water depth was obtained by summation of the height of the PT with respect to the sea bed and η_t . The height was measured by hand during low tide. Statistical wave parameters were obtained by computing a power spectrum on 15 minutes of water level data. The spectrum was calculated using a Hamming window with a window length of three minutes, using 50% overlap and giving 18 degrees of freedom. From these spectra a spectral moment is calculated using:

$$m_n = \int_0^\infty f^n S_p(f) df \quad (45)$$

Here, f^n is the frequency of the oscillation of water surface elevation and S_p is the variance density for a specific frequency. The spectrum was divided in low frequencies ($0.005 - 0.05 \text{ Hz}$) and high frequencies ($0.05 - 1 \text{ Hz}$). The significant wave height of the sea/swell waves was calculated from the spectral moment of the high frequencies ($m_{0,HF}$) using

$$H_s = 4\sqrt{m_{0,HF}} \quad (46)$$

Linear theory provided the additional parameters such as wave amplitude (U_w), orbital excursion length (d_0), and the mobility parameter (ψ).

EMF signals were stored in mV which were calibrated and rotated to give cross-shore (u) and alongshore (v) velocities in meter per second. The wave direction was obtained from these cross-shore and longshore velocities by performing a principal component analysis (PCA) on the high frequencies of the velocity data and taking the orientation of the first eigenvector of the u - v covariance matrix. The direction of the current was obtained by taking the fourth quadrant inverse tangent of the longshore and cross-shore velocities. These directions, with their magnitude, were already shown in the wave and current rose plot in Figure 19. The position of a point in the rose indicates the direction of the current. The distance of the point with respect to the center of the rose denotes the waveheight (m) or current strength (m/s) for the waves and currents, respectively. The rose clearly indicates that

the strongest current velocities were attained when the direction is nearly parallel to the orientation of the shoreline.

3.3.2 Bed stress computations

The effect of the waves, currents and combined action of waves and currents on the bed is expressed by the shear stress exerted on the bed. Calculations of the skin friction shear velocity and bed stress for combined conditions were carried out following the method of Grant and Madsen (1986), from here on referred to as GM86. The GM86 model calculates the friction factor and skin-friction shear velocities for wave, current, and combined conditions. The combined friction factor used in this model is given by an iterative process and is calculated as follows

$$\frac{1}{4\sqrt{f_{cw}}} + \log \frac{1}{4\sqrt{f_{cw}}} = \log \left(\frac{C_r u_b}{\omega z_0} \right) - 1.65 + 0.24(4\sqrt{f_{cw}}) \quad (47)$$

Where C_r is a coefficient that denotes the relative wave and current stress, u_b is the bottom current velocity, ω the radial frequency and the physical bottom roughness is given by (8) and relates to z_0 through $k_s = 30z_0$. $f_{cw} = 6.0 * 10^{-3}$ if there is no wave action and pure current action is assumed. The thickness of the wave-current boundary layer is calculated as

$$\delta_{cw} = \frac{2\kappa u_{*cw}}{\omega} \quad (48)$$

where the von Karman constant $\kappa = 0.40$. Eventually the skin-friction shear velocities are derived. The current shear velocity is given by

$$u_{*c} = \sqrt{0.5 * f_{cw} * u_{\delta}^2}, \quad (49)$$

where u_{δ} is the unidirectional velocity at the top of the wave-current boundary layer (δ_{wc}). The wave shear velocity is calculated with

$$u_{*w} = \sqrt{0.5 * f_{cw} * U_w}, \quad (50)$$

where U_w is the maximum orbital velocity at the top of the wave-current boundary layer. The combined shear velocity is calculated through

$$u_{*cw} = \sqrt{1} * u_{*w} \text{ or } u_{*cw} = u_{*c} \text{ if } \delta_{cw} < z_0 \quad (51)$$

Subsequently, the non-dimensional bed shear stress induced by waves, currents and combined flow are given by their Shields numbers (θ_w , θ_c , and θ_{wc} , respectively), calculated with equation (5).

3.3.3 Sonar image processing

The data of the sonar was stored as a backscatter intensity signal (Figure 22a). Acoustic noise, caused by high sediment concentration clouds and reflection of the water surface (a double bottom), was excluded from the data. Whilst processing, the quality of the backscatter signal was checked. Images that exhibited an interruption of the backscatter signal due to emergence of the sonar above the water were excluded for further processing if the interruption occurred on more than roughly 30% of the scan lines. Images were also excluded from further processing if the bed was poorly detected due to intense turbulence or very high suspension concentrations.

The position of the bed with respect to the sonar was determined for every scan position by identifying the position of the maximum backscatter intensity. The result was a bathymetry stored in spherical coordinates. These spherical coordinates were converted in to data points in Cartesian space for further processing (Figure 22b). The data was linearly detrended and data points that were more distant than 3.5σ (σ is the standard deviation of surface elevation) to the mean were removed. Here, 3.5 is a trial-and-error based value that turned out to be appropriate. A Digital Elevation Model (DEM) of the seabed was created using a locally weighted quadratic polynomial regression method (LOESS) (Figure 22c). In this method the data is first subsampled to a regular one millimeter spaced grid after which the elevation data is smoothed by fitting a quadratic model to localized subsets of the data. For this regression method the smoothing parameter was set to 0.15, signifying that the subset of data used for the fit comprises $0.15*n$ data points, where n is the total amount of data points. Because a quadratic model is fit to the subset, every feature smaller than half the smoothing parameter is removed. A larger smoothing scale produces a smoother surface and will make the crests of the bedforms less spiked. However, setting the smoothing scale to large may remove important features (small ripples).

The sonar performed most of the time rather poor in detecting the bottom at the edge of the scanned surface. This is probably caused by the larger distance between measuring head and object, increasing the chance of noise to occur. Because the edges of the DEMs were based on erroneous measurements the DEMs showed distinct peaks at the edge. To overcome this problem the DEMs were overlain by a circular mask that contributed $0.8*radius$ of the scanned surface (Figure 22d). The data not covered by this mask was not used for further data analysis, that is, bedform classification and bedform geometry calculations.

Bedform geometry was extracted from the masked DEMs. Bedform dimensions were determined as an average value for one DEM, so for 15 minutes of hydrodynamic data. Ripple height was calculated as (Austin et al., 2007):

$$\eta = 2\sqrt{2}\sigma \quad (52)$$

Here, σ is the standard deviation of surface elevation. Ripple spacing (λ) was determined visually from the DEMs and could only be derived for the small-scale 2D bedforms. This was done by averaging the length over the total amount of 2D ripples that could be identified in a DEM. Bedform orientation could not accurately be determined from the sonar images because the majority of the images did not show a coherent direction of crestlines (or the spatial scale of the scanned surface was not large enough to discover this). Bedform migration was also disregarded from this study because the temporal scale (15 min) of consecutive sonar images was too large for this purpose, i.e., the bedforms migrated outside the scanned surface.

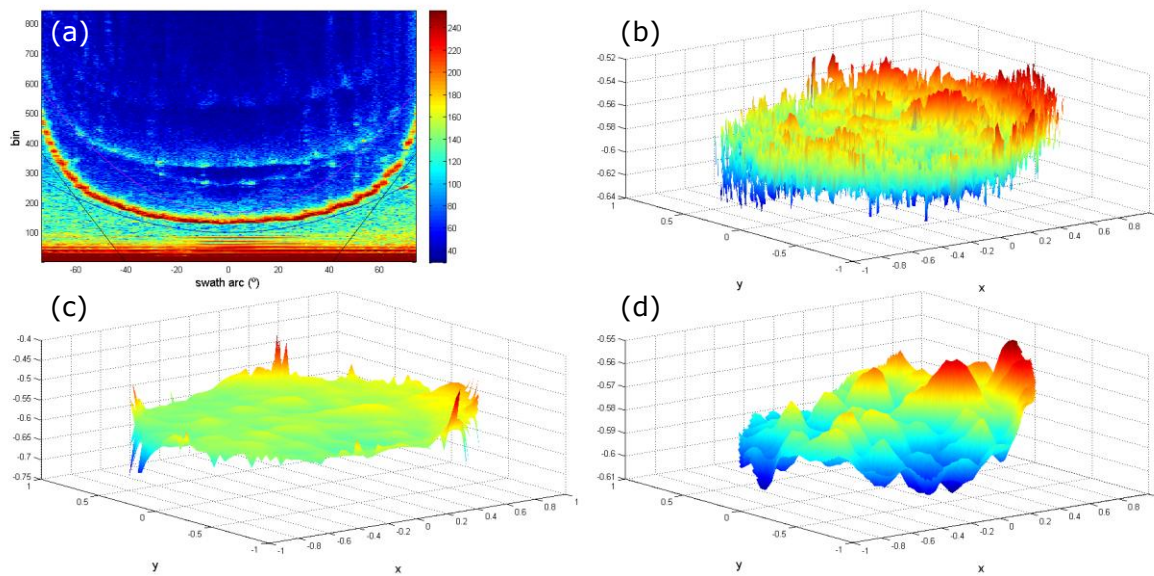


Figure 22: Step-wise visualisation of the 3DSRPLS data processing; a) plot of the backscatter intensity for one scan line, the maximum backscatter between the two functions indicates the position of the sea bed; b) surface plot of all raw bed elevation points when data is already detrended and outliers ($> 3.5\sigma$) are removed; c) smooth surface obtained with the quadratic LOESS filter; d) circular mask ($0.8 \cdot \text{radius}$) from (c). The image in (d) is used for bedform classification and extracting ripple dimensions.

3.3.4 Bed state classification

The bedform state was determined visually (i.e., subjectively) from the DEMs of the seabed. The classification criteria were established on the basis of size (small-scale versus large-scale) and configuration (two dimensional versus three dimensional), which is loosely based on the classification diagram of Dumas et al. (2005) (Table 1). The term small-scale versus large-scale was approached qualitatively because bedform length was not available for all the images. If multiple successions of bedforms could be distinguished in an image it was designated small-scale. If only one wavelength or part of a bedform wavelength could be distinguished, it was designated as large-scale. These divisions

led to four bed states: small-scale 2D ripples, small-scale 3D ripples, large-scale bedforms, and super-positioned small-scale ripples on large-scale bedforms.

Figure 22 gives examples of the four bed states distinguished in the sonar images with their characteristic morphology. Small-scale 2D ripples are characterized by joint ripple crests and troughs with multiple successions in an image. Bifurcations were present at some of the DEMs. A 2D visualization, a cross-section, can describe the full morphology of a single bedform. An example of small-scale 2D ripples is shown by Figure 22a.

Small-scale bedforms with a patchy appearance were classified as small-scale 3D ripples. The crests of these bedforms is somewhat less sharp than the small-scale 2D ripples and the size can be larger. The term 3D refers to dimensions needed to describe the full morphology of a single bedform. An example of small-scale 3D bedforms is given by Figure 22b.

Bedform features that were captured only partly by the DEM were classified as large-scale bedforms. In these images only a slope, crest or trough of the bedform was usually captured. No further distinction was made between the large-scale features because the size of the sonar images was not large enough to make a separation. Consequently, bedform length could not be derived for this class of bedforms. A large-scale bedform is shown in Figure 22c.

At times, a succession of small-scale bedforms developed on the crest, in the trough or on the slope of a large-scale bedform. These successions were classified as super-positioned bedforms. This depicts a super positioned small-scale bedform on the larger scale bedforms. An example of super-positioned bedforms is given in Figure 22d.

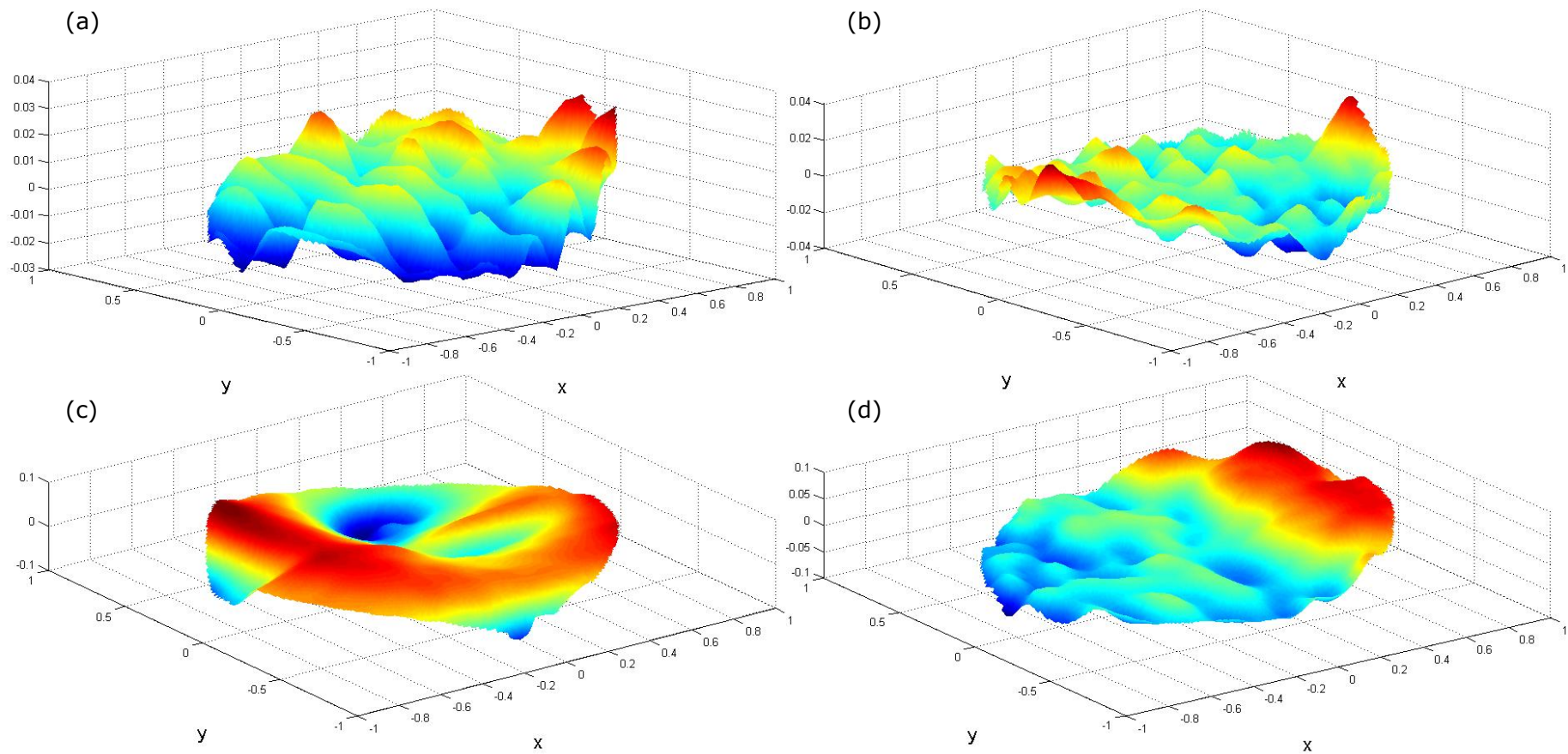


Figure 23: Example images of the classified bed states; (a) small-scale 2D ripples, (b) small-scale 3D ripples, (c) large-scale bedforms, and (d) superpositioned small-scale bedforms on a large-scale bedform.

4 Results

4.1 Time series of hydrodynamics, bed stress, and morphology

The 15-minute burst averaged main hydrodynamic dataset that is used in this research is shown in Figure 24. The data is plotted against a campaign time axis in hours. Here, zero hour corresponds to 1 October 2013 at 00.00 hour and 756 hour corresponds to 1 November 2013 at 12.00 hour. During this period the offshore significant spectral waveheight, $H_{1/3,off}$, ranged between ~ 0.5 to ~ 5.5 m (Fig. 24a) with mean wave periods, $T_{m,off}$, between 3 and 9 s (Fig. 24b). The spectral significant sea/swell wave height, $H_{1/3}$, at the frame varied between 0.01 and 1.1 m (Fig. 24c). Measurements are not continuous because all the measurement systems were switched off when the float emerged above the water during low tide. The variation in water depth is given in Figure 24d and ranged between 0.1 and 2 m. Panels c and d show that $H_{1/3}$ is modulated by the tide which indicates that the frame was located well in-to the surf zone and hence, the short waves approaching the frame were surf zone bores. The relative wave height, $H_{1/3}/h$, ranged between ~ 0.02 to ~ 1.1 (Fig. 24e), which is an indication of the relative cross-shore position. In this plot, the region of fully broken waves ($0.5 < H_{1/3}/h$) is separated from the breakpoint region ($0.4 < H_{1/3}/h < 0.5$) and non-breaking waves ($H_{1/3}/h < 0.4$) (Masselink et al., 2007). Although these boundaries should not be considered as robust thresholds between breaking and non-breaking, they are an indication for the likelihood that waves are breaking.

Figure 24f shows burst averaged cross-shore $\langle u \rangle$ and longshore $\langle v \rangle$ velocities, as recorded by the upper EMF (EMF2). Wave direction is plotted on a secondary axis. Positive cross-shore velocities were seaward directed and positive longshore velocities were directed to the north. The range of the cross-shore velocity varied from -0.51 to 0.27 m/s and the longshore velocities vary between -1.38 to 1.57 m/s. Wave direction ranged between 250° and 310° . Longshore velocities were strongest when a high-energy wave climate corresponded with a wave direction that was not shore normal ($\sim 280^\circ$, Fig. 19). Another mechanism that caused a longshore current was the tidal flow. However, the strength of this current was minimal when compared to the longshore current that was provoked by oblique incident waves. This can be seen during periods of low-energy wave conditions, when longshore flows were weak (e.g., at ~ 180 , ~ 290 , and 710 h).

Bed stress, as calculated with the GM86 model, is shown in Figure 24g. The three components of bed stress are given. The current shear stress, θ'_c , ranged from 0 to 1, the wave shear stress, θ'_w , from 0 to 0.7, and the combined shear stress, θ'_{cw} , varied between 0 and 1.3. Wave-induced bed stress was strongest during periods of high-energy wave conditions and current-induced bed stress was strongest during periods of strong (positive and negative) longshore flows, which was usually during the same periods as more intense wave breaking, during high-energy wave conditions, caused a stronger longshore flow. These events are, for example, well presented at ~ 230 , 400 , 490 , 550 , and 650 h.

Figure 24h shows the bedform types found and the coloured line at the bottom of the figure indicates the morphological setting surrounding the frame at that time. Blue signifies that the tripod was

situated in an intertidal channel, landward of a sandbar and seawards of the beach. The red color indicates that the tripod was on a sandbar, which was either on the crest, on the seaward slope, or on the landward slope of the bar. During the green period the frame was located on the landward side of a depression between two bars (a rip current mouth). Two blank periods are shown. Here, the surrounding morphology could not be determined because the tripod was submerged even during low tide. The bedform types are indicated by the black dots. The four different bedform types that were recognized from the sonar images occurred for every morphological setting during the experiment. Bed state data is absent for ~75-350 h and after ~650 h. The reason for this is that the dataset obtained by the sonar covers only a time period of 14 days due to a malfunctioning of the device from the 3rd until the 12th day of the campaign and a malfunctioning that arose on the 27th of October, during the preamble of the storm on the 28th of October. Moreover, there is not a sonar image for every 15 minute burst of hydrodynamic data because the sonar was mounted fairly high above the bed and consequently was submerged later during rising water and emerged earlier during falling water. Bedform height ranged between ~0.1 to ~0.12 m (Fig. 24i) and attained peak values during the preamble of the 28th October storm. Bedform length is not displayed in this plot due to the limited amount of measurements.

4.2 The bedforms

4.2.1 Occurrence and characteristics

The bedforms found during the experiment are listed in bar graphs, separated for each morphological setting surrounding the frame (Fig. 24). For 336 of the sonar images the quality was well enough to give a good representation of the sea bottom and consequently made it possible to classify the bedforms in the image to one of the four bedform types. As reported earlier, the sonar did not operate during the entire experiment. This fact has to be kept in mind for the correlation of bedform type to morphological setting, because the counts of specific bedform types do not only depend on the morphological setting but also on the fact if the sonar was operating during a specific time-interval. The bedform type of small-scale 3D ripples was most abundant during the experiment (149 times, 44%). The occurrence of small-scale 2D ripples accounts for 13% (43 times) of total bed states found. Large scale bedforms contributed to 36% (122 times) of all the bed states and the bedform class of super-positioned small-scale ripples on larger scale bedforms was found 22 times (7%). The distributions of the counts of bedform types for each morphological setting are quite similar. Small-scale 3D ripples and larger scale bedforms are the dominating type of bedform class, 2D small-scale bedforms occurred less, and super-positioned bedforms were rarely found.

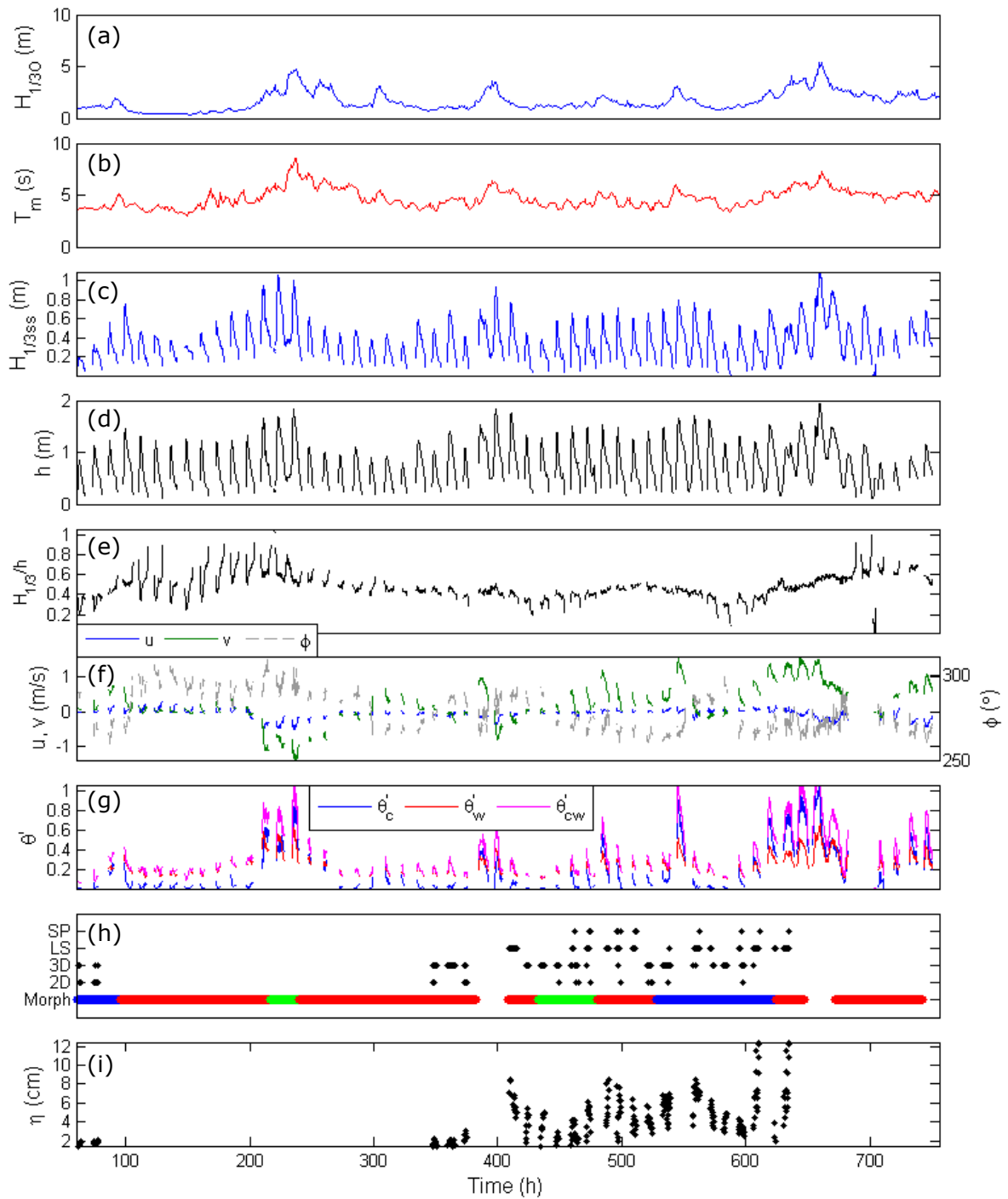


Figure 24: Time series of: Offshore (a) significant spectral waveheight $H_{1/3,off}$; (b) mean wave period $T_{m,off}$; and local (c) spectral significant sea/swell (0.05 – 1 Hz) wave height $H_{1/3}$; (d) water depth h ; (e) ratio of sea/swell waveheight to waterdepth $H_{1/3}/h$; (f) mean cross-shore $\langle u \rangle$ and along-shore $\langle v \rangle$ velocities and wave direction (Φ); (g) total bed stress (Shields numbers) induced by currents (blue), waves (red), and combined waves and currents (magenta); (h) bedform type and morphological setting, indicated by the coloured line: blue = intertidal channel, red = intertidal bar, and green = rip-current mouth; [f] bedform height η .

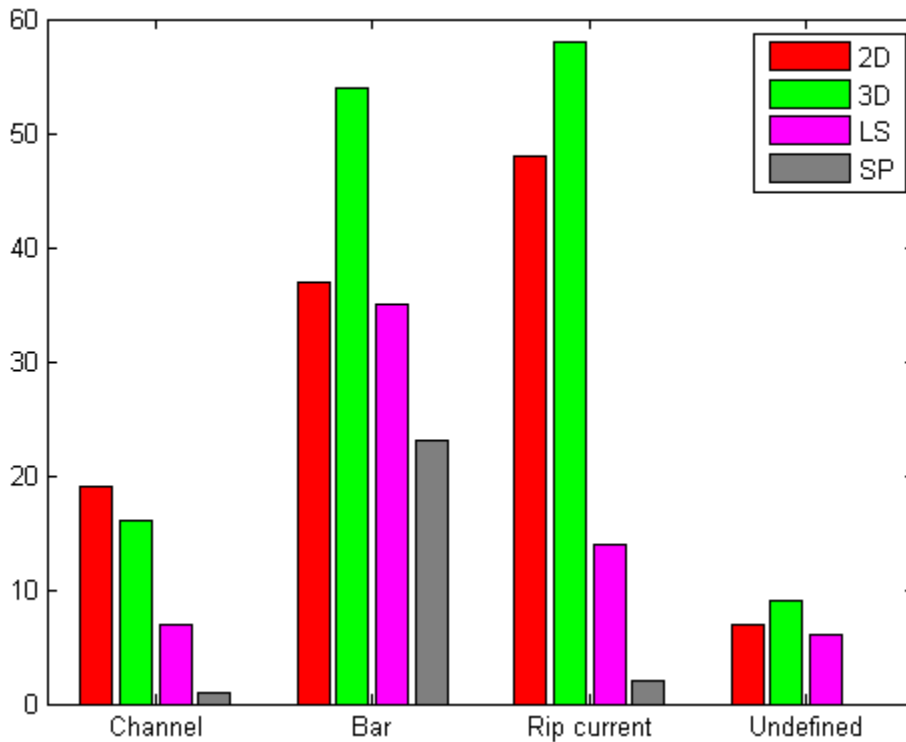


Figure 25: Bed state occurrence histograms, separated by morphological setting. Small-scale 3D bedforms (3D), small-scale 2D bedforms (2D), large-scale bedforms (LS), and super-positioned small-scale ripples on larger scale bedforms (SP).

The bedforms found could all be characterized by a formative hydrodynamic property (wave-current shear stress) and a geometric property (bedform height). The distributions of these parameters are shown for the four bedform types separately in box-whisker plots (Fig. 25a and b). Inside the boxes the center line indicates the median or 50th percentile (Q_2) of that class. The boxes to the left and right of the median represent the first (Q_1), or 25th%, and third (Q_3), or 75th%, quartiles, respectively. The whiskers in these plots extend to the largest and smallest measurement that is still within 1.5 times the nearest interquartile range. The interquartile range is the difference between the third and first quartile ($Q_3 - Q_1$). The plusses are points that are omitted from the box because they are more distant from the nearest quartile than 1.5 times the interquartile range.

The boxes in Figure 26a indicate that the distributions of θ'_{cw} differ for every separate class of bedform types. The class of small-scale 2D bedforms has the smallest values of bed stress and the large scale bedforms are formed during the strongest bed stress. The other two classes have bed stress values that fall in between the extremes of the 2D and LS classes. The distributions are different for each class, yet, the distributions in θ'_{cw} overlap considerably between the classes. This overlap was also found by Dolphin and Vincent (2009), who plotted their bedform classes against the combined Shields parameter as well. They used different classes for their bedforms but their short wave ripples and (2D and 3D) long wave ripples are comparable to the present 2D and LS class, respectively. The

range of the distributions in wave-current shear stress for these bedform types in Dolphin and Vincent (2009) is similar to the range found here.

The distributions of bedform height are visualized in a similar manner (Fig. 26b) and also shows a different distribution for each class. Comparable to Figure 26a the distribution in bedform height shows considerable overlap between the bedform type classes as well. Furthermore, the figure shows a very large range of bedform heights for the class of large scale bedforms. This may indicate a misinterpretation of large scale bedforms because these bedforms are not expected to have bedform heights similar to small-scale 2D and 3D ripples.

Because the distributions show considerable overlap (Fig. 26a and b), t-tests on the equality of means are performed on the samples to indicate if the difference between the means of the samples are significantly different. This testing was done with a 95% confidence level ($\alpha = 0.05$) and with the assumption that the variances of the (unknown) populations are equal. Table 2 lists the descriptive parameters and the values of the test statistic t that resulted from these tests. The critical t value (t_{crit}) for these tests was (close to) 1.96, due to the large number of observations. For every distribution of θ'_{cw} and η the (absolute) value of the test statistic t is larger than t_{crit} . This means that the difference between the means of the samples is not statistically significant.

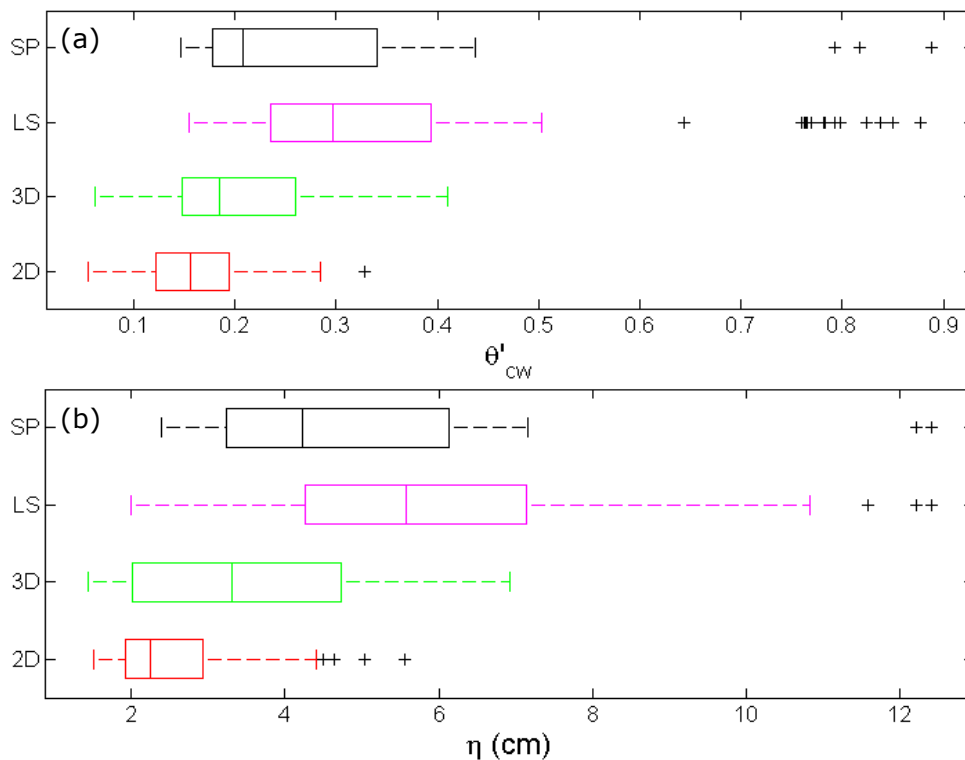


Figure 26: Box-whisker plots separately for each class for (a) the combined non-dimensional shear stress and (b) the bedform height

Table 2: Descriptive statistics for the four bedform types and results of t-tests

Type	n	\bar{X}	s	SSE	t		
θ'_{cw}					3D	LS	SP
Small-scale 2D	38	0.1578	0.0625	0.0101	-3.51	-6.48	-3.85
Small-scale 3D	143	0.2059	0.078	0.0065		-8.72	-4.15
Large-scale	120	0.3509	0.1799	0.0164			-4.12
Super-positioned	20	0.3142	0.2369	0.053			
η					3D	LS	SP
Small-scale 2D	43	2.6	0.9892	0.1508	-3.44	-10.18	-5.14
Small-scale 3D	149	3.4	1.5424	0.1264		-11.35	-3.95
Large-scale	122	5.9	2.0759	0.1878			-6.53
Super-positioned	19	5.1	2.8933	0.6169			

Shear stress is a common used parameter in bedform geometry models and bedform height is usually a desired parameter to obtain with the model. However, the found bedform classes cannot be characterized by a specific bedform height or a specific shear stress distribution. This means that the models cannot be able to predict the bedform morphology (types) accurately. A plot of the bedform height versus the wave-current Shields parameter (Fig. 27) shows that there is no clear relation between these two parameters as well, implying that there is no linear relationship between forcing and geometry. The figure does show, however, that 2D ripples and large-scale bedforms plot in separate regions of the figure. This motivates for implementing the bedform observations in the wave and current stability diagram of Section 2.2.

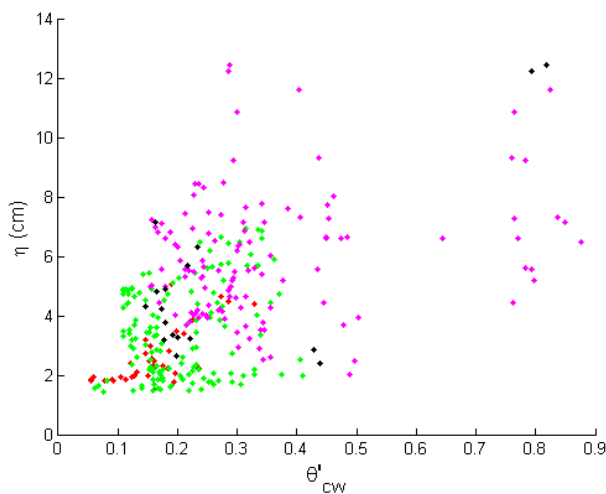


Figure 27: Bedform height and wave-current shear stress. Colour scale of bedforms classes is similar to Figure 25.

4.2.2 Generic classification

The classified bedforms are plotted in the wave and current shear stress stability diagram of Section 2.2 (Fig. 28) in an attempt to define hydrodynamic stability regions for the four bed states found. The bedform classes are colour-coded and the lines in the diagram give the (semi-empirical) boundaries for the stability fields (see caption).

The small-scale 2D ripples plot in a range varying from the wave-dominated to the combined flow part of the diagram ($0.05 < \theta'_w < 0.3$ and $0.002 < \theta'_c < 0.08$). This concentration in small-scale 2D bedforms decreases towards mixed flow conditions and the class is not present when the current induced shear stress increases over $\theta'_c \approx 0.08$. Furthermore, bedforms seem to evolve from 2D to 3D to large-scale when only wave action increases and current strength is very limited. In fact, the strength of the current in this region is so weak ($\theta'_c < 0.05$, below threshold of motion) that the current can be considered of no importance. The absence of 2D ripples in the region where current induced shear stresses are strong ($\theta'_c > 0.08$), suggests that the formation of small-scale 2D ripples is controlled by wave action but that a superimposed current can limit the formation of 2D ripples.

The 3D ripples are found over the entire range of the data in the diagram, i.e., they are present in the wave-dominant and mixed flow regime. The concentration of this bedform type is quite equally distributed through the diagram but is somewhat smaller for very moderate wave- and current conditions ($\theta'_w < 0.1$ and $\theta'_c < 0.01$). Small-scale 3D ripples are only non-existent during an high-energy wave-current climate (i.e., the region above the Allen-Leeder sheetflow criterion). The presence of 3D ripples under very weak current conditions indicates that 3D ripples can be formed by waves as well as by waves and currents together. Unfortunately, no measurements were gathered during current dominant conditions, that is, in the stability region between the line of equality and the current-dominance threshold.

The largest concentration in large-scale bedforms is found near the region of equal wave and current strength ($\theta'_w \approx \theta'_c$, the dashed line of equality in Fig. 28a). This is a region of a high-energy wave-current climate and hence, explains why the bedforms are large. These events of strong current-induced shear stress occur only when a strong long-shore current is present (Fig. 24f and g). The concentration in the large-scale bedform class (LS) decreases considerable when current induced shear stress is below the threshold of motion ($\theta'_c < 0.05$) and is almost non-existent during pure wave conditions. The class co-exists with the 3D ripples, that is, they occur during similar hydrodynamic conditions, not simultaneously in time. The LS class is also well presented above the sheetflow threshold, where flatbed is expected. Apparently, this criterion is not appropriate for the investigated environment. Because the large-scale bedforms are so numerous near the one-to-one line, this bed state class can be considered as bedforms that are formed when currents and waves both influence bedform formation on the field site studied.

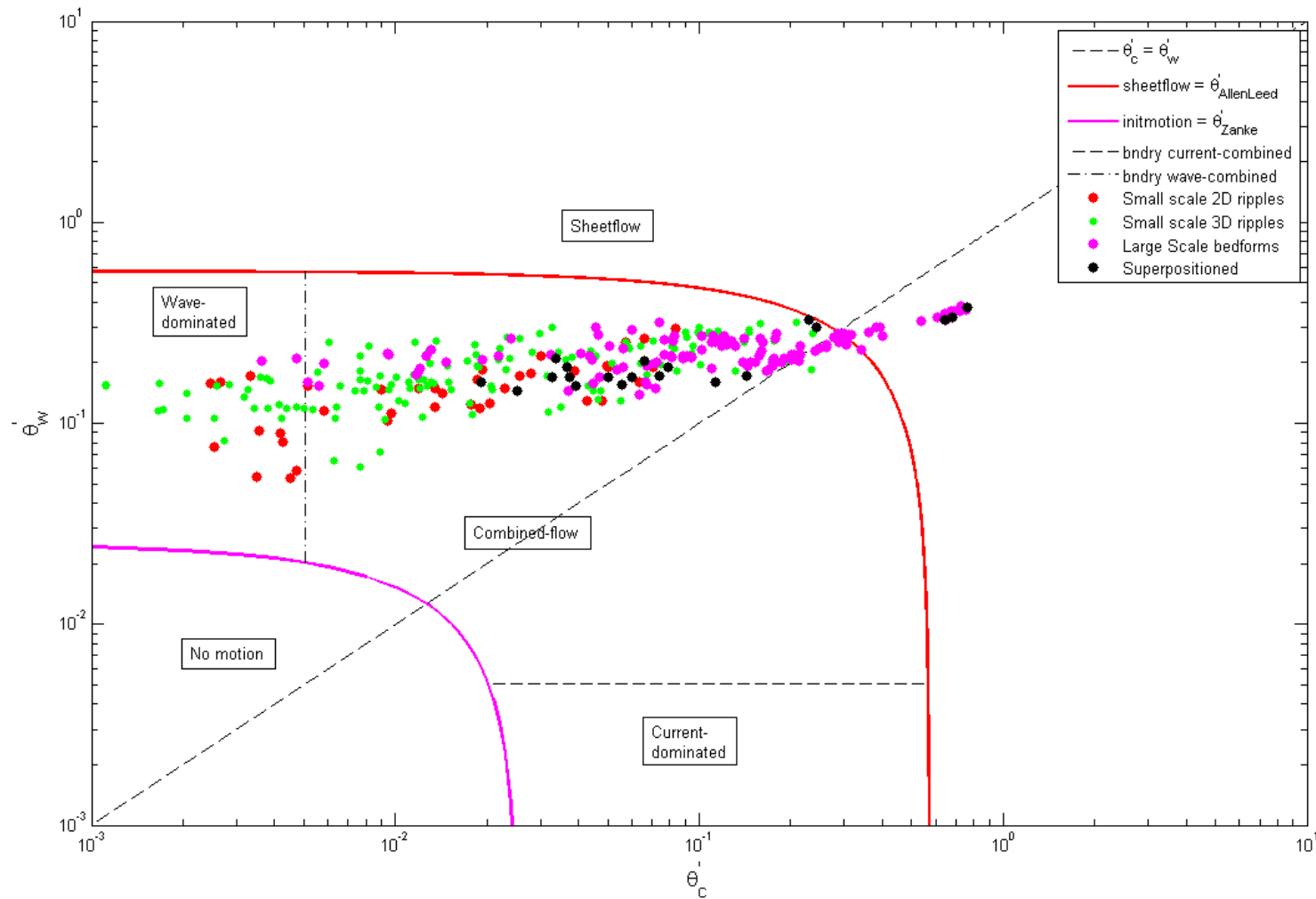


Figure 28: Bed state stability diagram of the wave Shields number and current Shields number. Black dashed line gives the 1:1 relationship of equal strength of θ'_c and θ'_w , Horizontal dashed and dashed-dotted line give areas of current-domination and wave-domination, respectively. Threshold values for these areas are based on Kleinhans (2005) and lie at $0.2\theta'_{zanke}$. Magenta line indicates the threshold for the initiation of motion, given by the Zanke (2003) model (equation 13). The transition to Upper Stage Plane bed is described by the empirical formula of Allen and Leeder (1980), described in equation 15.

The class of super-positioned bedforms is mainly concentrated between the 2D ripples and large-scale bedforms and the range of the data does not vary substantially in θ'_c and θ'_w , though in a few cases $\theta'_c \approx 1$. The limited range of conditions suggest that formative conditions for super-positioned bedforms are quite specific. The next section will elaborate further on this.

The class of small-scale 2D ripples is mainly located in the wave-dominant part of the diagram in Figure 28. This suggests that the formation of small-scale 2D bedforms is mainly controlled by wave action, and not by the combination of waves and currents. Therefore, it is informative to place the 2D ripple observations with-in the Clifton and Dingler (1984) classification schemes for wave-formed ripples of Section 2.4.1 (Fig. 29a and b). An advantage of these classification schemes is that they include the geometric properties of the ripples (in contrast to Fig. 28). In these diagrams, the measurements of this study are plotted together with a large quantity of wave-formed bedform measurements. The sources of these bedform measurements are listed in Table 1 of Goldstein et al. (2013) and comprise field as well as laboratory (wave flume, oscillating tunnel, and wave racetrack) data.

Figure 29a shows that the bedform length measurements of 2D ripples fall well within the range of the larger dataset, which suggests that they are in the approximate right order of magnitude. However, it also illustrates that the range of conditions is relatively small when compared to the Goldstein et al. (2013) dataset. The linear relationship of λ/D with d_o/D that is present in the Goldstein et al. (2013) dataset is not obvious for the present measurements due to this small range of hydrodynamic conditions. Additionally, the diagram shows that the present 2D observations are sub-orbital ripples. This corresponds to the observations of Masselink et al. (2007), who found sub-orbital ripples in the shoaling and surf zones of a macrotidal coarse grained beach at Sennen Cove.

Figure 29b shows ripple steepness with normalized orbital excursion length (d_o/D). The horizontal dashed line lies at $\eta/\lambda = 0.15$ and signifies the threshold for vortex ripples (Bagnold, 1963). The small-scale 2D ripples are located well in-to the post-vortex regime and therefore, are not steep ripples. This does not correspond to Clifton and Dingler (1984), who found that post-vortex ripples are usually anorbital. Moreover, the steepness values of the present measurement are rather low when compared to the larger data set (i.e., the ripples are fairly flat). This may indicate that bedform height is somewhat small or that bedform length is somewhat large for the 2D ripples.

Alternatively, the geometry of the bedforms is scaled with the wave Mobility number parameter (Eq. 27) (Fig. 29a-c), which is used in the Nielsen (1981) and Grasmeijer and Kleinhans (2004) bedform predictors (Sect. 2.4.2). Again, the measurements are plotted with the Goldstein et al. (2013) data set to make comparison easier. In Figure 29c the small-scale 2D ripples are separated from the large scale bedforms at $\psi \approx 10$. Grasmeijer and Kleinhans (2004) found, on the same field site, that bedforms generally changed from small wave ripples (SWR) for small mobility numbers to large wave ripples (LWR) for larger mobility numbers. Their SWR and LWR might be comparable to the 2D and LS

class in this study, respectively. Furthermore, Fig 29c shows that all observations fall within the range of the wave-formed Goldstein et al. (2013) dataset. This indicates that the formation of the bedforms of the present study is mainly controlled by waves. Figures 29d and e indicate again that ripple steepness is somewhat small when compared to the Goldstein et al. (2013) data, and that ripple length, when scaled to A_{orb} , is somewhat large. This suggests that rather ripple length than ripple height is the less reliable geometric parameter. Next to these observations the Figures 29c-e indicate that a clear relationship of geometry with ψ is hard to define for the present dataset, due to the limited range of hydrodynamic conditions.

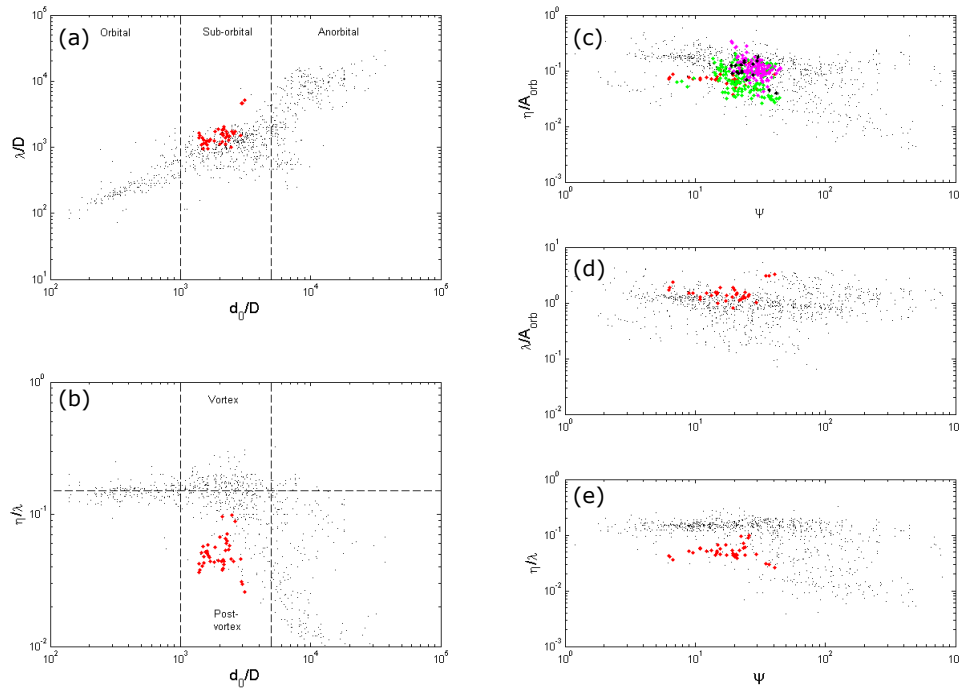


Figure 29: Bedform observations together with the Goldstein et al. (2013) dataset placed in the Clifton and Dingler (1984) classification schemes (a and b), and scaled with the wave Mobility parameters (c to e).

4.3 Bedform dynamics

4.3.1 Bedform response

The wave-current induced shear stress and the orbital excursion were shown to be useful parameters for the classification of sand ripples in the nearshore zone (Fig. 28 and 29a and b). The development of these hydrodynamic forcing parameters, and the resultant bedform geometry and type, will be discussed further for individual tidal cycles. For each of the three different morphological settings two typical tides are plotted, where time is relative to high tide, and forcing and bedform parameters are normalized by their high tide value (Fig. 30). The field site is characterized by an asymmetric tide which is shown by the fast rising waters and long duration of the ebb stage (Fig. 30a-c and m-o). This causes an asymmetric distribution of water levels around high tide. The distribution of the induced

wave-current shear stress usually shows a clear tide-modulated behaviour as well, which is asymmetric due to the short duration of the flood stage and long duration of the ebb stage. The peak values are usually attained at or just before high tide (Fig. 30d, e, p, q). When the frame was located in an intertidal channel the distribution of the wave-current shear stress through the tidal cycle was considerably different (Fig. 30f and r). This is presumably due to the influence of long-shore currents. After all, the effect of a super-imposed long-shore current is expected to be of larger importance in a channel than on an intertidal bar or in a cross-shore oriented rip channel mouth. The orbital excursion is modulated by the tide as well and also shows an asymmetric distribution around high tide (Fig. 30g-i and s-u). The development of bedform height shows a cycle of growth and destruction for every tide. However, the peak values of this cycle are usually not attained at high tide, when the values of wave-current shear stress and orbital excursion are largest. The bedforms continue to grow and attain peak values approximately ~ 0.5 h after high tide. Hence, the cycle of growth and destruction of bedforms lags on the forcing parameters (θ'_{cw} and d_o). After the stage of growth, the height of the bedform sometimes stabilizes and shows a post-high-tide arrested development (Fig. 30k and w) or decreases immediately (Fig. 30 j, l, and v). This cycle of bedform growth and destruction is less well pronounced for tide 4, which also showed a different behaviour of the shear stress development.

The sequence in development of bedform types is more or less similar for tide 20a, 20b, and 25b, which occurred when the tripod was located in a rip channel mouth and in an intertidal channel. During low energetic conditions small-scale bedforms develop, towards high tide these bedforms evolve in larger scale bedforms until conditions become less energetic and small-scale bedforms develop on top of the larger bed features. By the end of the ebb stage the larger scale features are totally reworked and only small-scale bedforms are present. These three tides, that have a characteristic tide-modulated sequence in bedform type development, also show a pronounced post-high-tide arrested development of bedform height, in contrast to the three other tides that do not show the emergence of large scale bedforms. Notable is that the development of bedform types on an intertidal bar does not show the typical tide-modulated sequence. This suggests that local morphology affects flow patterns in such a way that it influences the development sequence of bedform types.

The typical tide-modulated sequence in bedform development, from small-scale ripples in to larger scale bedforms and back to small-scale bedforms again, is particularly well shown by tide 20a and totally absent for tide 15, although both tides show a clear tide-modulated behaviour of θ'_{cw} and d_o . Furthermore, tide 20a is characterized by a well pronounced post-high-tide arrested development of bedform height and tide 15 is not. This makes these particular tidal cycles most suitable for investigation of the forcing parameters that cause (the absence of) these features. Time-series of the development of the hydrodynamic forcing parameters are shown in Figure 31: shear stress (Fig. 31a and b), relative waveheight, waveheight, and orbital excursion (Fig. 31c and d), and mean current strength and the angle between waves and currents (Fig. 31e and f).

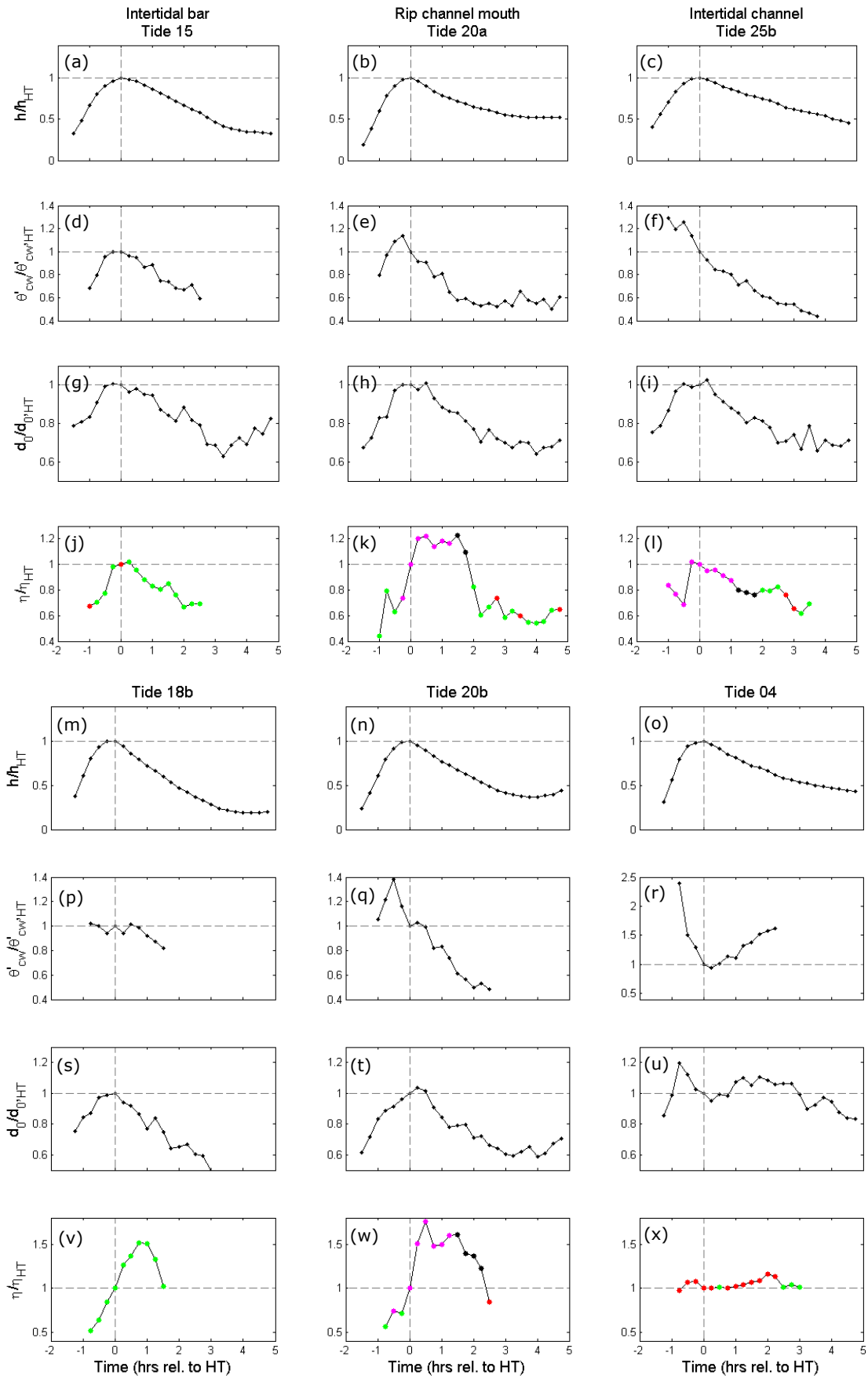


Figure 30: Tidal development of waterdepth (a-c, m-o), wave-current shear stress (d-f, p-r), orbital excursion (g-i, s-u), and bedform height (j-l, v-x), all normalized by their high tide (HT) value. Six typical tides are shown for different morphological settings: an intertidal bar, a rip channel mouth, and an intertidal channel (After Austin et al., 2007).

The flood stages of both tides show an increase in all forcing parameters (increase in the wave-current energy climate). Around high tide, peak values of stress are attained that correspond with a peak in wave intensity and current strength. Yet, the peak in stress is considerably larger for tide 20a and shows the development of large scale bedforms. The difference in wave height is small between the two tides, and the larger peak in stress seems to be caused by the current, which is factor ~ 3 stronger during tide 20a than for tide 15. The large scale bedforms evolve into super-positioned small-scale ripples on top of these larger scale bedforms. This is accompanied by a drop in current strength (Fig. 31e). Notable as well is that this transition from LS to SP to small-scale ripples seems to be accompanied by a transition from the break-point region to non-breaking waves (Fig. 31c). During the final ebb stage the bedforms are reworked into small-scale bedforms. During this transition the strength of the current (θ'_c , Fig. 31a) decreases below a value of 0.05 and can be considered of minor importance. During both tides the angle between waves and currents changes from perpendicular to nearly parallel (Fig. 31de). This is presumably due to a change in current direction, which is highly dependent on the local morphology.

4.3.2 Tidal relaxation

Figure 30 showed, next to a difference in the sequence in bedform development between different tides, that some tides show an arrested development of bedform height after high tide. The tides that comprehend a continuous dataset of bedform measurements and showed a tide-modulated distribution of wave-current stress around high tide are plotted in θ - η space in order to highlight the trajectory of bedform height with respect to forcing during a tidal cycle. The trajectories are shown to emphasize if the geometry of the bedforms is subjected to hysteresis effects. These hysteresis effects would be visible as a non-linear response of geometry with forcing, i.e., an equal increase and decrease in forcing would not have a similar effect of growth and destruction on ripple height. The plots are shown in Figure 32. Here, the combined Shields number is normalized with the value that is present at high tide (θ'_{cwHT}) and the same procedure is used for the bedform height (η_{HT}). This is done because the absolute values of θ'_{cw} and η may vary considerably between tides, which makes comparison harder. The trajectories are separated by morphological setting.

Figure 32a shows the θ - η trajectories of two tides that occurred when the frame was located on an intertidal sandbar. The two tides show an increase and decrease in forcing (combined shear stress) as well as in bedform height. The increase in forcing is accompanied by a corresponding increase in bedform height. The subsequent decrease in bedform height, however, lags on the decrease in forcing.

Shear stress decreases after high tide (tide 16b) but bedform height does not return to pre-high-tide values. Bedform height values of tide 15 do return to initial values eventually but this takes some time. The tides in Figure 32c show this lag in ripple height destruction even more clearly. Figure 32b and d do not show the profound increase in θ'_{cw} and η during the rising water stage. The figures do show, however, that a decrease in θ'_{cw} after high tide may be accompanied by a very small decrease (or even an increase) in bedform height.

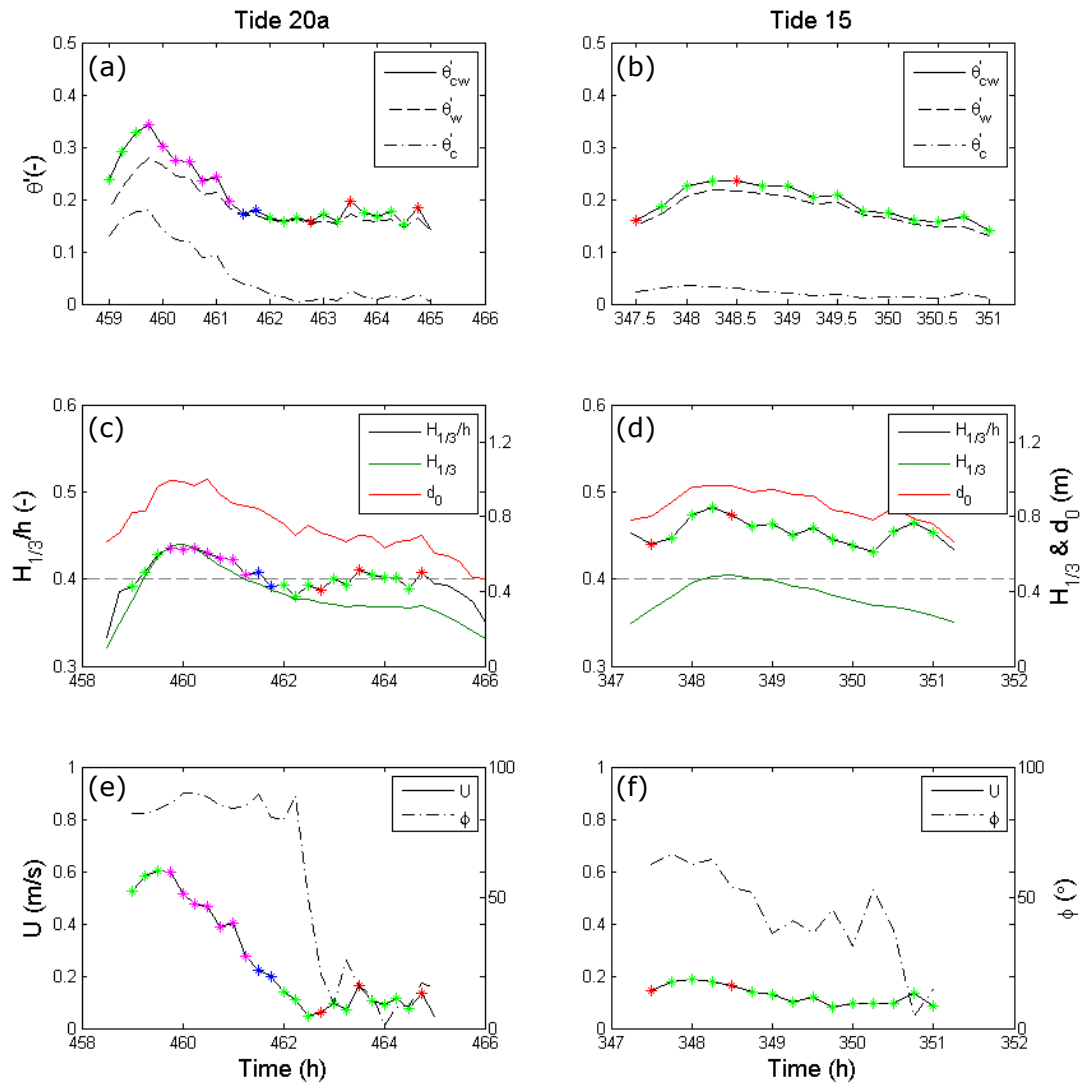


Figure 31: Development of hydrodynamics of tide 20a and 15; (a,b) development of bed stress, (c,d) sea/swell waveheight, relative waveheight, and orbital excursion diameter, (e,f) mean velocity and angle between waves and currents.

The trajectories of bedform height are different for every tide but the general trend is as follows: at the beginning of the tide η is smallest, towards high tide θ'_{cw} increases with a corresponding increase in η , after high tide ($\theta'_{cw}=1$ and $\eta=1$ in the plots) θ'_{cw} decreases until a value that is smaller than at the

beginning of the tidal cycle. Bedform height, however, lags on this decrease in forcing, and only starts to decrease after a while. This means that during the falling stage of a tidal cycle a decoupling of forcing and geometry occurs. This decoupling of forcing and geometry signifies that the geometry of the bedforms not only depends on the prevailing hydrodynamic conditions but also depends on the previous hydrodynamic conditions and the previous bedform configuration. This observation indicates the importance of hysteresis effects for the morphology of the bedforms.

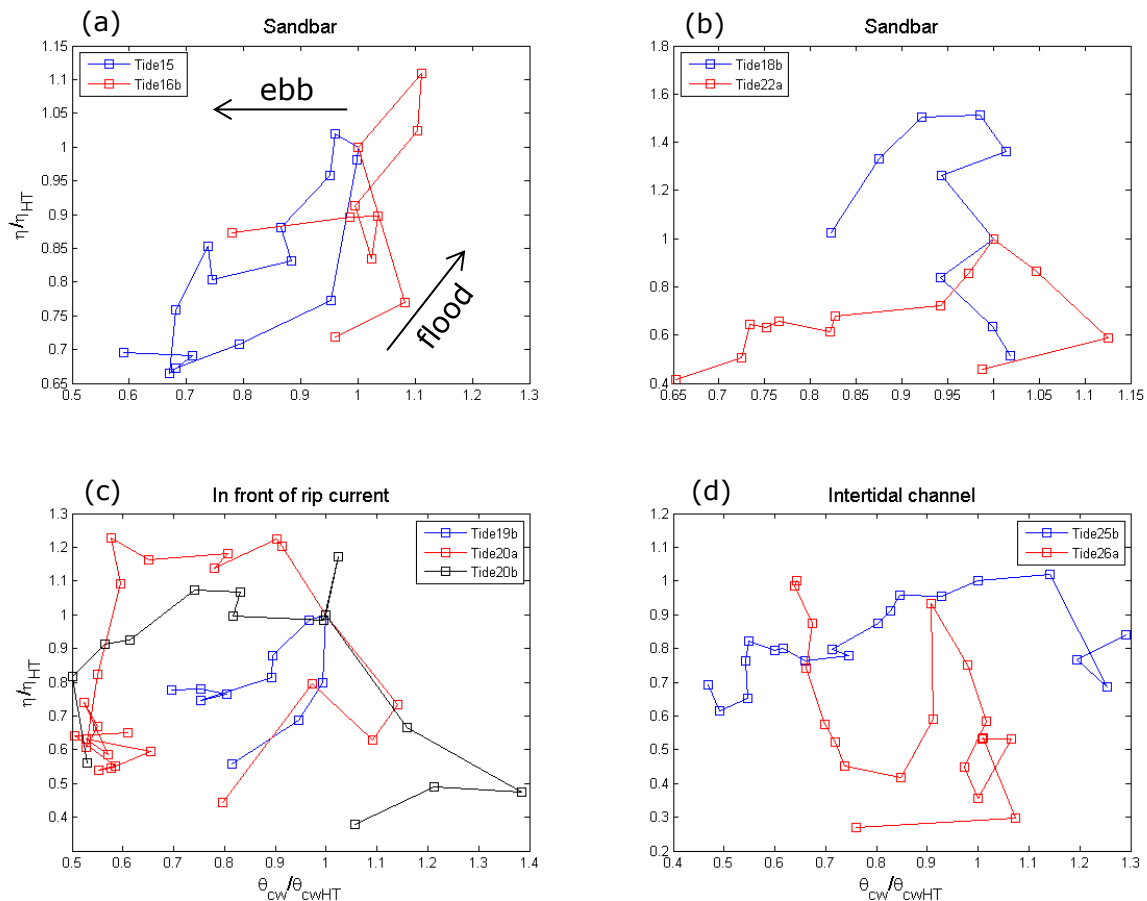


Figure 32: Development of bedform height through a tidal cycle. Bedform height is normalized with the bedform height that was present during high tide (η_{HT}) and combined shear stress is normalized with the shear stress present during high tide (θ_{HT}) (after Austin et al., 2007).

4.4 Equilibrium observations

Previous section showed that hysteresis effects (tidal relaxation or history effects) are important for the geometry of the bedforms. It signifies that (a part of) the bedforms cannot be related directly to the hydrodynamic conditions that were present during that specific time because the bedforms are formed during an earlier stage. This explains partly the reason that the distribution in θ'_{cw} showed considerable overlap between the different bedform type classes (Fig. 25) and that the segregation of bedform types was rather poor in the bed state stability diagram (Fig. 28), because this diagram is

only valid for equilibrium morphology. A re-evaluation of the segregation of bedform types should provide better results if only bedforms are implemented that are in equilibrium with the flow. This is complicated by the fact that it is impossible in a natural hydrodynamic environment to reveal when the duration of the flow is long enough for equilibrium morphology to be attained. However, Figures 30 and 32 indicate that lag effects are most likely to occur during the ebb stage of a tidal cycle. Implementing only the flood stage bedform observations in the diagram would presumably give better results in segregation. A re-evaluation of the bed state stability diagram with the data separated by the flood and ebb stage observations is shown in Figure 33. The diagram with the flood stage observations still shows considerable overlap between the bedform types (Fig. 33a). Clearly, this diagram does not show a clear segregation of the different bedform types even for the flood stage observations. Any reduction in scatter in the diagram in Fig. 33a with respect to Fig. 33b is likely due to the decrease in data points, because the flood stage is of shorter duration than the ebb stage.

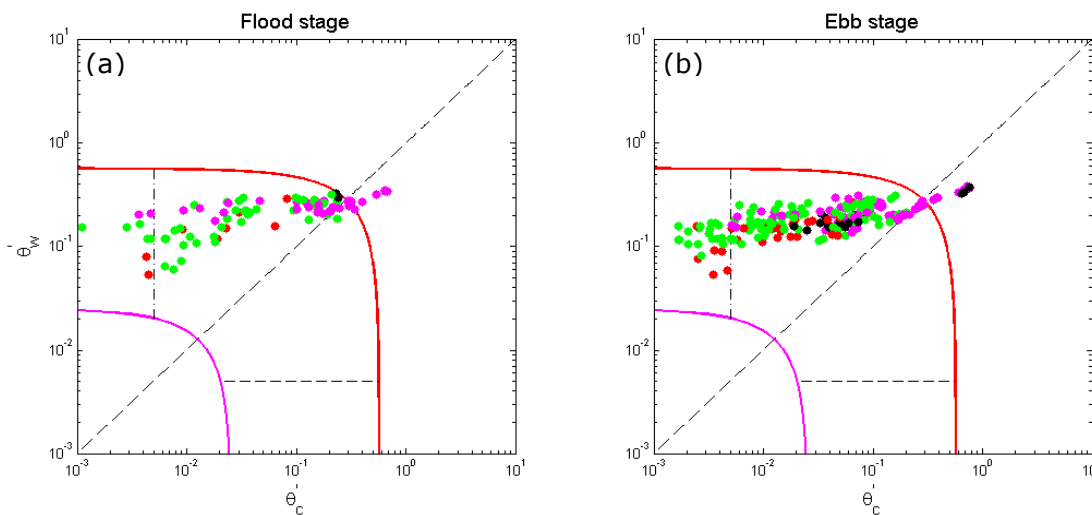


Figure 33: Re-evaluation of Figure 28 with flood and ebb stage observations separated.

4.5 Predicting bedform dimensions

The four bedform geometry predictors described in Section 2.4.2 were programmed and tested. Of these four predictors, two predictors are developed for wave-formed bedforms and two predictors for the formation of bedforms under wave-current conditions. The four different models are all developed to predict equilibrium morphology. Because it was shown that the geometry of the bedforms can be subjected to lag effects (and so are not in equilibrium with the flow), these predictors are not expected to give a very accurate prediction of bedform geometry. Yet, because previous section showed that a separation in flood and ebb stage observations does not separate observations that are in equilibrium from observations that are out of equilibrium, there was no reason to adopt this division for the prediction of bedform geometry. Because equilibrium predictors are relatively simple to incorporate

in models and do not require strong computational power it is still informative to test these predictors for the present dataset.

The accuracy of the predictors is shown for bedform height (Fig. 34a, c, e, and g) and for bedform length of the 2D ripples (Fig. 34b, d, f, and h). A quantification of the error of the predictions is given by the standardized error variance (SEV), which is the residual variance scaled by the variance in the observations. The standardized error variance is given by

$$SEV = \frac{\sum(x_{obs} - x_{pred})^2}{\sum(x_{obs} - \bar{x}_{obs})^2} \quad (53)$$

Here, x_{obs} is η or λ as measured from the DEMs and x_{pred} is η or λ calculated with one of the four predictors.

The N181 wave predictor (Eq. 28 – 30, Fig. 34a and b) is shown to give an over-prediction of bedform height for small-scale 2D ripples and an under-prediction for the large scale bedforms. Bedform length is predicted reasonably well but under-predicts as well. Two observations of bedform length are under predicted by a factor of ~10.

The GK04 predictor (Eq. 31 – 33, Fig. 34c and d) is an empirical predictor based on a dataset acquired on the same field site and is therefore expected to perform well. The predictor performs slightly better than the N181 predictor (smaller SEV values for bedform height and length), however, shows similar features for under- and over-prediction for the different bedform types.

For the calculation of the Li96 predictor (Eq. 35 – 40, Fig. 34e and f) it is assumed that $\theta_{wm} = \theta'_w$. The wave-current bedform predictor performs best for bedform height and is the only predictor that gives predictions for bedform height that result in a standardized error variance with is lower than one (SEV = 0.82). Particularly the large scale bedforms are better predicted by this predictor, though scatter is still significant. For the prediction of bedform length the performance is rather poor and under-predicts by a factor 2-3.

The wave-current KO00 predictor (Eq. 41 and 42, Fig. 34g and h) shows the best results for the prediction of bedform length (SEV = 0.68) and only fails to predict two distant measurements well. Because these two measurements are predicted very poor with every predictor they can be considered as outliers. The predictor performs worst for the prediction of bedform height with values that are over-predicted up to a factor ~5.

The standardized error variance values show that the Li96 predictor performs best for bedform height and the KO00 predictor performs best for bedform length. When a model has to be considered that performs best for both bedform height and length (e.g., for practical applications) the SEV values indicate that the GK04 predictor is the most appropriate choice.

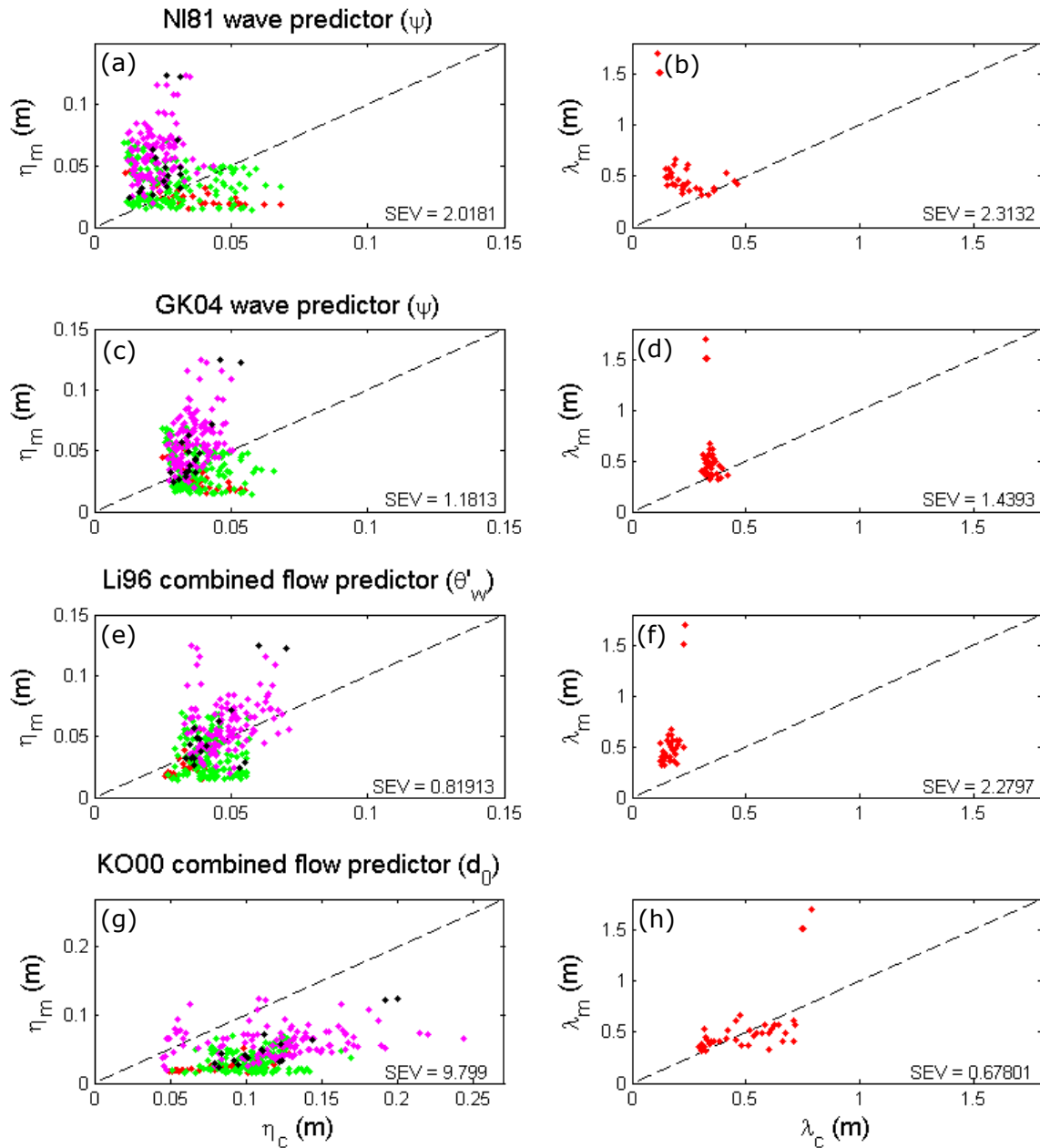


Figure 34: Accuracy of four bedform geometry predictors. Dashed black lines are one-to-one lines of perfect agreement, observations are colour-coded similar to Fig. 25. (a, b) Nielsen (1981) wave bedform predictor, (c, d) Grasmeyer and Kleinhans (2004) wave bedform predictor, (e, f) Li et al. (1996) wave bedform predictor, and (g, h) Khelifa and Ouellet (2000) wave-current bedform predictor.

5 Discussion

I found that bedforms that are formed on the intertidal stretch of a sandy beach, with median grain diameter of 330 μm , can be classified as small-scale 2D ripples, small-scale 3D ripples, large-scale bedforms and super positioned small-scale ripples on large-scale bedforms. These four different bedform types are characterized by a unique distribution of combined shear stress (θ'_{cw}) and bedform height (η), although the distributions overlap considerably between these classes. The unique distributions in combined shear stress signify that each class of bedform type is characteristic for a specific wave-current energy climate. The bedform configuration (type) is in principle dependent on the relative contribution of the influence of waves and currents, expressed with the Shields number. The absolute strength of these components determines the size of the bedforms. Small-scale 2D ripples are only present under moderate wave conditions with limited ($\theta'_c < 0.1$) influence from a current and small-scale 3D ripples are present under moderate wave conditions and a large range of current stresses ($0.001 < \theta'_c < 0.3$). The large scale bedforms are present when the waves and currents act with roughly equal magnitude ($\theta'_c \approx \theta'_w$), which is during energetic conditions in the present environment. During the course of a tidal cycle the strength of the forcing parameters increases during the flood stage, to attain peak levels around high tide. When the influence from the current is of sufficient strength, bedforms evolve from small-scale ripples in to large scale bedforms. The transition from small-scale ripples in to larger scale bedforms around high tide is accompanied by a corresponding increase in bedform height. Consequently, peak values in bedform height are attained around high tide as well. During the ebb stage the large scale bedforms are reworked in to small-scale ripples again. During this stage, stresses decrease but bedform height remains stable for a while and shows a post-high tide arrested development. Consequently, the decrease in bedform height lags on the decrease in forcing, which causes a decoupling of forcing and resultant bedform geometry. This decoupling of forcing and bedform configuration causes a part of the bedform observations to be out of equilibrium with the flow. The relaxation time of the bedforms is presumably the reason that the distributions in combined shear stress overlap (Fig. 26a), the cause that the bedform types in the stability diagram are not clearly separated (Fig. 28), and probably the main reason for the disability of equilibrium bedform predictors to predict the geometry very accurately (Fig. 34).

The ranges of combined shear stress found for the different bedform classes correspond to the ranges found by Dolphin and Vincent (2009) in their field experiment at Noordwijk aan Zee (in ~14 m water depth), although they classified their bedforms differently. The range of the present 2D small-scale ripples ($0.05 < \theta'_{cw} < 0.3$) is almost similar to the range of their Short Wave ripples ($0.07 < \theta'_{cw} < 0.3$) and the range of the present large scale bedforms ($0.15 < \theta'_{cw} < 0.9$) corresponds closely to the ranges of their 2D and 3D Large Wave ripples together ($0.07 < \theta'_{cw} < 0.8$). Their distributions showed considerable overlap as well. Next to that, they placed their bedform observations in the θ'_c -

θ'_w stability diagram and found overlap between the bedform types as well. They discuss that this overlap is due to a number of factors:

- the relaxation time of the bedforms cause them to be out of equilibrium (history effect),
- multiple bedform types can exist at the same time,
- and the limited range of the sonar can lead to mis-interpretation of bedform types.

The co-existence of multiple bedform types in a DEM is partly covered in this thesis by use of a 'super-positioned' bedform class, yet a clear definition of small-scale 2D or 3D ripples was sometimes difficult. The morphology of the bedforms was seen to be most affected by relaxation time effects during the flood stage. Nonetheless, did a separation of flood- and ebb stage data not result in an improvement of the stability diagram (Fig. 33a).

Despite the overlap between the bedform classes in the stability diagram, the observations for the separate bedform classes correspond to those found by Arnott and Southard (1990). They concluded from their lab experiments that their 2D ripples were stable under low oscillatory and unidirectional velocities and that with increasing either of the velocity components the configuration becomes progressively 3D. Furthermore, they found that these 3D ripples were stable at low to moderate oscillatory velocities and under a wide range of unidirectional velocities.

The characteristic bedform type that was found for combined flows ($\theta'_c \approx \theta'_w$) is totally different to the bedforms found by Amos et al. (1988). They found distinct super imposed patterns of small-scale current and small-scale wave ripples with a ripple height of 0.2 cm and spacing of 20 cm. They conducted the experiments in fine sand (230 μm) and 22 m waterdepth. The wave-current ripples found in this study have a ripple height which is $O(10)$ larger. The larger water depth is most likely the main explanation for the difference in observed patterns. The combined flow pattern of small-scale current and small-scale wave ripples was not observed because wave and currents were only present in equal magnitude during energetic (stormy) conditions. The characteristic combined flow ripple formations, as described by Amos et al. (1988) were, however, seen in the field as relict ripples. Therefore it can be reasoned that these bedform configurations are formed during the last stage of the tide when wave and currents are moderate, but present at equal strength.

The present observations of bedforms in a nearshore environment provide insight for a crude attempt to define stability regions for the bedform classes. This attempt is shown in Figure 35. In this diagram a stability region for the equilibrium morphology of 2D ripples is shown by the red ellipsoid. The ellipsoid ranges from very calm pure wave conditions to more moderate combined flow conditions. More intense pure wave conditions were found to produce 3D ripples and/or large-scale bedforms. The 3D ripple stability region is indicated by the green ellipsoid and is stretched over a large range of θ'_c . I do think that this ellipsoid can even be stretched to a broader range of θ'_w to include the entire region between wave dominant and current dominant conditions, because pure unidirectional flows were also found to produce 3D patterns by Arnott and Southard (1990). The purple ellipsoid gives the stable region for the large-scale bedforms. Although the LS class was also found at lower θ'_c , the class

is not assumed to be stable here because Figure 31 showed that lag effects are most prone to occur when large scale bedforms develop. Furthermore, it showed that the transition from LS to SP to small-scale ripples is accompanied by a strong decrease in current strength. Therefore these measurements are thought to be relict features of more energetic conditions. The super positioned class is not indicated because this class cannot be considered to be a stable bedform class. The hydrodynamic conditions that are present during the SP class are formative for small-scale ripples but it is the presence of the ‘old’ LS bedforms that alters the configuration.

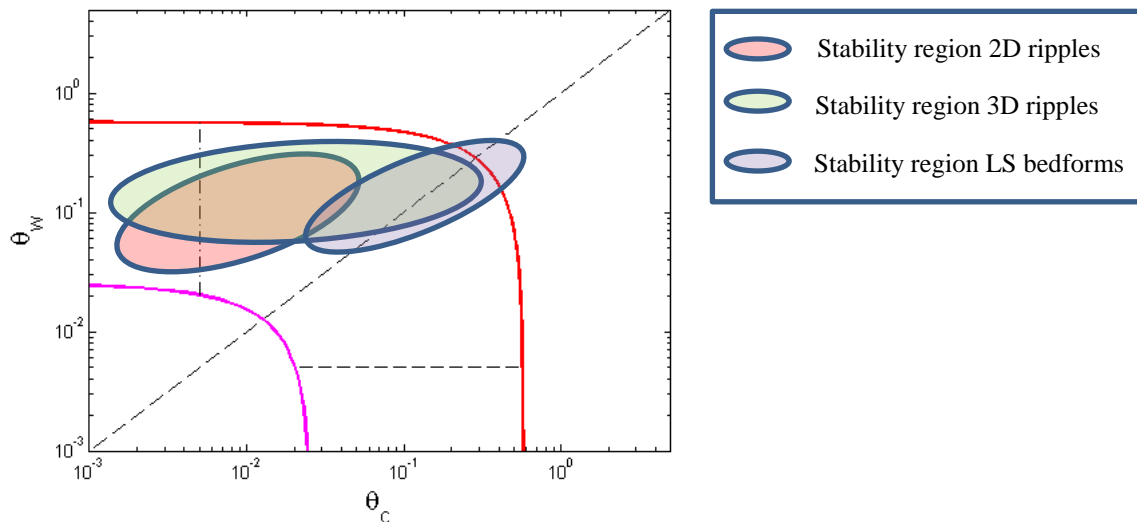


Figure 35: Bed state stability regions in the $\theta_c - \theta_w$ combined flow stability diagram for a nearshore environment.

The tide-modulated sequence of bedform development (Fig. 31) is most comparable to the observations of Hay and Mudge (2005). They found a repeated bed state storm cycle of bedform growth from an initial irregular ripple state, to cross ripples, to linear transition ripples, and then to flat bed, followed by a reverse sequence during wave decay. Although no real storm events are included in the present research, it was found that a sequence in bedform development from small-scale ripples to larger scale bedforms and back again to small-scale ripples is only present when certain peak values in stress are reached and absent if hydrodynamic conditions are moderate. The sequence of bed states found during the built-up of a moderate storm by Li et al. (1998) showed that during storm decay lunate mega ripples developed. The spatial scale of the DEMs was not large enough in the present research to reveal the morphology of the large scale bedforms but they might have been lunate mega ripples because Lanckneus et al. (1999) also found lunate mega ripples on the Egmond aan Zee field site.

The post-high tide arrested development of bedform geometry that was found in Figure 30 was already recognized by Austin et al. (2007). They analyzed the relaxation time of wave ripples on a tidal beach with comparable hydrodynamic conditions ($H_{1/3} = 1-2$ m and $h = 1.3 - 3.3$ m). They found a clear symmetrical tide-modulated behaviour of θ_{cw} and d_0 around high tide, with bedform height

and length stabilizing during the ebb stage as well. They discuss that the tide modulates the hydrodynamic conditions at a rate that is far more rapid than the relaxation time of the ripples. Because they found a linear response between forcing and geometry during the flood stage, they discussed that their flood tide ripples should be near equilibrium. Nonetheless, they observed the breakdown of two equilibrium predictors (Wiberg and Harris, 1994 and Williams, 2004) for the flood tide ripples as well. They discussed that this was probably attributed to the surf zone origin of their data, because the increased non-linearity and near-breaking wave conditions are very different to those of the shoaling wave and continental shelf conditions from where those two models have been primarily formulated. The cause for the overlap between the flood stage data in the stability diagram (Fig. 33a) is most likely similar to this. The diagram is mainly tested for laboratory and large water depth field data.

The ranges in bedform height of the different bedform classes are comparable to the wave-formed ripples observed by Grasmeyer and Kleinhans (2004), which was on the same field site. The present observations of ripple height vary between 0.01 m and 0.12 m and their ripples varied between 0.007 - 0.10 m. Because the field site is similar to Grasmeyer and Kleinhans (2004) and the ranges in bedform height are comparable, this suggests that the GK04 predictor should perform quite well for the present dataset. The predictor performs reasonably well for bedform height but the Li et al. (1996) shows a better performance. This difference is probably attributed to the difference in the hydrodynamic parameters on which the models are based. Bedform geometry was, after all, seen to show a better relation with stress than with the mobility parameter. Notable is that Grasmeyer and Kleinhans (2004) had better results of predicting the dimensions if Large Wave Ripples (LWR) were left out consideration. The present performance of the GK04 predictor also shows that the predictor performs worst for the LS class. The shortcomings of the predictors signify that further development of geometry predictors for nearshore environments (like tidal beaches) should incorporate the effects of relaxation time effects.

Summarizing the findings of this thesis I can state that the behaviour of bedforms in a nearshore sandy environment highly depends on the (relative) magnitude of waves and currents, giving different configurations for specific wave-current climates. Thereby, causes the relaxation time of the bedforms (together with the fast changing hydrodynamic conditions) a decoupling of forcing and geometry, which is most pronounced during the ebb stage of a tide. This decoupling of forcing and geometry is the main reason for the break-down of equilibrium bedform predictors in natural occurring nearshore environments.

6 Conclusions

A one month field work was conducted on a median coarse grained sandy beach near Egmond aan Zee in order to measure hydrodynamics and bathymetry. The sonar images acquired during this field work were used to classify the bathymetry on the beach in to four bed state classes. The geometry was extracted from these images.

The type of bedforms found in this study are: small-scale 2D ripples, small-scale 3D ripples, large-scale bedforms and super positioned small-scale ripples on large-scale bedforms. These four classes are all characterized by a different distribution of θ'_{cw} and η , although distributions overlap considerably.

During the course of a tidal cycle, the increase in forcing during the flood stage will cause the bedforms to evolve from small-scale in to larger scale bedforms if a current of sufficient strength is present. This transition is accompanied by a corresponding increase in bedform height. The fast changing hydrodynamics and the relaxation time of the bedforms will cause a decoupling of forcing and geometry during the ebb stage.

The tested equilibrium predictors perform reasonably well. The combined flow predictors are shown to perform slightly better. The out-of-equilibrium state of the bedforms is the main reason for the disability of equilibrium bedform predictors to give a very accurate prediction of bedform geometry. Observed difference in performance between the models is attributed to the hydrodynamic parameters on which the model is based.

The main goal of this thesis was to investigate the effect of a nearshore environment on the dynamics of bedform morphology. This can be described as follows: the configuration of bedforms in the intertidal zone depends on the relative contribution of waves and currents and the size depends on the strength of the wave-current energy climate. The fast changing hydrodynamics of a nearshore environment causes a decoupling of forcing and geometry due to the relaxation time of the ripples. This is most pronounced during the ebb stage when large scale bedforms are present.

Acknowledgements

First of all I want to thank the supervisors of this thesis, prof dr. Gerben Ruessink and prof. dr. Maarten Kleinhans, for guidance through the processes of data acquisition, analysis, and interpretation. Secondly I am grateful to the technical staff of the Department of Physical Geography for their help with deployment of the measurement frame and logistical issues during the fieldwork. Thanks go to Evan B. Goldstein, Giovanni Coco, and A. Brad Murray for using their large compiled bedform dataset. Furthermore I thank Laura Taal as fieldwork partner, other fellow students for having constructive discussions, Hessel Woolderink for his assistance with GIS, and Winnie de Winter for help during the writing process.

References

- Allen J. R. L. and Leeder, M. R., 1980.** Criteria for the instability of upper-stage plane beds. *Sedimentology* 27, 209-217.
- Allen, J. R. L., 1984.** Sedimentary structures, their character and physical basis. *Developments in Sedimentology* 30, I and II, Elsevier, Amsterdam, The Netherlands.
- Amos, C.L., Bowen, A.J., Huntley, D.A., Lewis, C.F.M., 1988.** Ripple generation under the combined influences of waves and currents on the Canadian continental shelf. *Continental Shelf Research*, 8, 1129-1153.
- Andersen, K.H. and Faraci, C., 2003.** The wave plus current flow over vortex ripples at an arbitrary angle. *Coastal Engineering*, 47, 431-441.
- Arnott, R. W. and Southard, J. B., 1990.** Exploratory flow-duct experiments on combined flow bed configurations, and some implications for interpreting storm-event stratification. *Journal of Sedimentary Petrology* 60, 211-219.
- Austin, M.J., Masselink, G., O'Hare, T.J., Russel, P.E., 2007.** Relaxation time effects of wave ripples on tidal beaches. *Geophysical research letters*, Vol. 34.
- Baas, J.H., 1993.** Dimensional Analysis of Current Ripples in Recent and Ancient Depositional Environments. Ph.D. Thesis, University of Utrecht, The Netherlands, 199 pp.
- Baas, J.H., 1994.** A flume study of the development and equilibrium morphology of current ripples in very fine sand. *Sedimentology* 41, 185-209.
- Bagnold, R. A., 1963.** Beach and nearshore processes in *The Sea*, edited by M. N. Hill, pp. 507–553, Wiley-Interscience, New York.
- Bell, P.S., Thorne, P.D., Williams, J.J., 1998.** Acoustic measurements of sand ripple profile evolution under controlled wave conditions. *Proceedings*, 353–358.
- Bridge, J.S. and Best, J.L., 1988.** Flow, sediment transport and bedform dynamics over the transition from dunes to upper-stage plane beds: implications for the formation of planar laminae. *Sedimentology*, 35, 753-764.
- Carling, P.A., 1999.** Subaqueous gravel dunes. *Journal of Sedimentary Research* 69, 534-545.
- Carstens, M.R., Neilson, F.M., Altinbilek, H.D., 1969.** Bed Forms generated in the Laboratory under an Oscillatory Flow. C.E.R.C., Technical Memo 28, USA.
- Clifton, H.E., 1976.** Wave-formed sedimentary structures – A conceptual model beach and nearshore sedimentation, edited by Davies and Ethington, *Econ. Paleontol. Mineral. Spec. Publ.* 24, p. 126-148.
- Clinnton, H. E., Dingler, J. R. (1984).** Wave-formed structures and paleoenvironmental reconstruction, *Mar. Geol.*, 60, 165-198.
- Dumas, S., Arnott, R.W.C., Southard, J.B., 2005.** Experiments on oscillatory-flow and combined flow bed forms: implications for interpreting parts of the shallow-marine sedimentary record. *Journal of Sedimentary Research*, Vol. 75, No. 3, May, 2005, p. 501-513.
- Dolphin, T. and Vincent, D., 2009.** The influence of bedforms on reference concentration and suspension under waves and currents. *Continental Shelf Research* 29, 424 – 432.
- Doucette, J.S., O'Donoghue, T., 2006.** Response of sand ripples to change in oscillatory flow. *Sedimentology* Vol. 53, 581-596.
- Goldstein, E.B., Coco, G., Murray, A.B., 2013.** Prediction of wave ripple characteristics using genetic programming. *Continental Shelf Research* 71 (2013) 1 – 15.
- Grant, W. D., and O. S. Madsen, 1979b.** Bottom friction under waves in the presence of a weak current, NOAA Tech. Rep., ERL-MESA, 150 pp., Natl. Oceanic and Atmos. Admin.
- Grant, W. D., & Madsen, O. S., 1982.** Movable bed roughness in unsteady oscillatory flow. *Journal of Geophysical Research: Oceans*, 87(C1), 469-481. doi:10.1029/JC087iC01p00469

- Grant, W.D., and Madsen, O.S., 1986.** The continental-shelf bottom boundary layer. Annual Review of Fluid Mechanics. 1986. 18: 265 – 305.
- Grasmeijer, B. T. and Kleinhans, M. G. 2004.** Observed and predicted bed forms and their effect on suspended sand concentrations. Coastal Engineering 51, 351-371.
- Hay, A.E., and Mudge, T., 2005.** Principal bed states during SandyDuck97: Occurrence, spectral anisotropy, and the bed state storm cycle. Journal of geophysical research, Vol. 110.
- Inman, D.L., 1957.** Wave-generated ripples in nearshore sands. Tech. Memo 100, Beach Erosion Board, USA.
- Khelifa, A., Ouellet, Y., 2000.** Prediction of sand ripple geometry under waves and currents. Journal of Waterway, Port, Coastal and Ocean Engineering 126 (1), 14–22.
- Kleinhans, M.G., 2005.** Phase diagrams of bed states in steady, unsteady, oscillatory and mixed flows. Utrecht University.
- Li, M. Z., & Amos, C. L., 1998.** Predicting ripple geometry and bed roughness under combined waves and currents in a continental shelf environment. *Continental Shelf Research*, 18(9), 941-970. doi:10.1016/S0278-4343(98)00034-X
- Li, M.Z. and Amos, C.L., 1996.** Predicting ripple geometry and bed roughness under combined waves and currents in a continental shelf environment. *Continental Shelf Research* 18 (1998) 941-970.
- Li, M. Z. and Amos, C. L., 1998.** Field observations of bedforms and sediment transport thresholds of fine sand under combined waves and currents. *Marine Geology* 158, 147-160.
- Li, M. Z., Wright, L. D., & Amos, C. L., 1996.** Predicting ripple roughness and sand resuspension under combined flows in a shoreface environment. *Marine Geology*, 130(1–2), 139-161. doi:10.1016/0025-3227(95)00132-8
- Lyne, V. D., Butman, B., & Grant, W. D., 1990.** Sediment movement along the U.S. east coast continental shelf—I. estimates of bottom stress using the grant-madsen model and near-bottom wave and current measurements. *Continental Shelf Research*, 10(5), 397-428. doi:10.1016/0278-4343(90)90048-Q
- Masselink, G., Austin, M.J., O'Hare, T.J., Russel, P.E., 2007.** Geometry and dynamics of wave ripples in the nearshore zone of a coarse sandy beach. Journal of geophysical research, Vol. 112. doi: 10.1029/2006JC003839
- Miller, M.C., and Komar, P.D., 1980b.** Oscillation sand ripples generated by laboratory apparatus. *J. Sediment Petro.*, 50(1), 173-182.
- Miller, M.C., McCave, I.N. & Komar, P.D., 1977.** Threshold of sediment motion under unidirectional currents. *Sedimentology* 24, 507-528.
- Mogridge, G.R., and Kamphuis, J. W., 1972.** Experiments on bed form generation by wave action. Proc. 13th Conf. Coast. Engrg., ASCE, New York, 1123-1142
- Myrow, P. M. and Southard, J. B. 1991.** Combined flow model for vertical stratification sequences in shallow marine storm-deposited beds. *J. of Sedimentary Research* 61 (2), 202-210.
- Nielsen, P., 1981.** Dynamics and geometry of wave-generated ripples. *Journal of Geophysical Research* 86 (C7), 6467–6472.
- Pedocchi, F., & García, M. H., 2009.** Ripple morphology under oscillatory flow: 1. prediction. *Journal of Geophysical Research: Oceans*, 114(C12), - C12014. doi:10.1029/2009JC005354
- Ribberink, J. S., 1995.** Time-averaged sediment transport phenomena in combined wave-current flows. Part II, Report H1889.11, Delft Hydraulics, Delft, The Netherlands.
- Simons, D.B., and Richardson, E.V., 1965.** A study of variables affecting flow characteristics and sediment transport in alluvial channels. In: Federal Inter-Agency Sediment Conference 1963 Proceedings: US Department of Agriculture publication 970, 193-207.
- Simons, D.B., and Richardson, E.V., 1966.** Resistance to flow in alluvial channels. Geological Survey Prof. Paper 422-I, Washington, USA.

- Smyth, C.E. and M.Z. Li, 2005.** Wave-current bedform scales, orientation, and migration on Sable Island Bank. *J. Geophysical Research*, 110, doi:10.1029/2004JC002569.
- Soulsby, R.L., 1998.** *Dynamics of Marine Sands*. Thomas Telford, London.
- Soulsby, R.L., Whitehouse, R.J.S., 2005b.** Prediction of Ripple Properties in Shelf Seas. Mark 2 Predictor for Time Evolution. Report TR154, HR Wallingford, Wallingford, UK.
- Soulsby, R.L., R.J.S. Whitehouse, K.V. Marten, 2012.** Prediction of time-evolving sand ripples in shelf seas. *Continental Shelf Research*, 38, 47-62.
- Southard, J. B. and Boguchwal, A.L., 1990.** Bed configurations in steady unidirectional water flows. Part 2. Synthesis of flume data: *Journal of Sedimentary Petrology* 60, 658-679.
- Sternberg, R.W., 1972.** Predicting initial motion and bedload transport of sediment particles in the shallow marine environment. In: *Shelf sediment transport, process and pattern*, D. J. P. SWIFT, D. B. DUANE and O. H. PILKEY, editors, Dowden, Hutchinson and Ross, pp. 61-83.
- Swales, A., J.W. Oldman, K. Smith, 2005.** Bedform geometry on a barred sandy shore. *Marine Geology* 226. 243-259
- Tanaka, H., Dang, V.T., 1996.** Geometry of sand ripples due to combined wave– current flows. *Journal of Waterway, Port, Coastal and Ocean Engineering* 122 (6), 298–300.
- Tanaka, H. and N. Shuto, 1984.** Sand movement due to wave-current combined motion. *Coastal Engineering in Japan*, Vol. 27.
- Van den Berg, J.H. and Van Gelder, A., 1993.** A new bedform stability diagram, with emphasis on the transition of ripples to plane bed in flows over fine sand and silt: *Special Publications of the International Association of Sedimentologists* 17, 11-21.
- Van den Berg, J.H. and Van Gelder, A., 1998.** Discussion: Flow and sediment transport over large subaqueous dunes: Fraser River, Canada. *Sedimentology* 45, 217-221.
- Van Rijn, L.C. 1984.** Sediment transport, part I: bed load transport, *J.of Hydraul. Eng.* 110(10), 1431-1456.
- Van Rijn, L. C., 1993.** *Principles of sediment transport in rivers, estuaries and coastal seas*, Aqua Publications, Oldemarkt, The Netherlands.
- Wiberg, P.L., Harris, C.K., 1994.** Ripple geometry in wave-dominated environments. *Journal of Geophysical Research* 99 (C1), 775–789.
- Yalin, M.S., 1985.** On the determination of ripple geometry. *Journal of Hydraulic Engineering*, Vol. III, No. 8.
- Yokokawa, M., 1995.** Combined flow ripples: Genetic experiments and application for geologic records. *Mem. Fac. Sci., Kyushu Univ., Ser. D, Earth Planet. Sci., Vol. XXIX, No. 1*, pp. 1-38.
- Young, J.S.L. and Sleath, J.F.A., 1990.** Ripple formation in combined transdirectional steady and oscillatory flow. *Sedimentology* 37, 509 – 516.
- Zanke, U.C.E. 2003.** On the influence of turbulence on the initiation of sediment motion, *International J. Of Sediment Research* 18(1), 1-15.

Websites:

<http://argus-public.deltares.nl/archive/>. Accessed throughout the fieldwork.